Experimental study on the correlation between depolarization ratios and lidar ratios of cirrus clouds over Leipzig, Germany with the lidar systems BERTHA and Polly^{XT}

DIPLOMARBEIT

submitted on January 23, 2013

Fakultät für Physik und Geowissenschaften der
Universität Leipzig

Name:	André Klepel
Matrikelnummer:	9925070
Studiengang:	Diplom-Physik
Betreuer:	Dr. Dietrich Althausen und Prof. Dr. Friedrich Kremer
Erstgutachter:	Prof. Dr. Friedrich Kremer
Zweitgutachter:	Prof. Dr. Andreas Macke

Contents

1 Introduction

Ice containing clouds in the upper troposphere play a key role in Earth's radiation budget. This considerable influence is due to their high incidence around the globe, their optical depths, and due to their scattering properties. Satellite data show an average cirrus cloud globe cover of at least 30% (Wylie et al., 1994). Cirrus clouds reflect parts of incident solar radiation back to space and also parts of emitted terrestrial radiation back to Earth. Their incidence, altitudes and optical properties leads to either warming or cooling. The scattering behaviour of ice crystals alters with shape and size. Thus, it is essential to measure the micro-physical properties, such as crystal shapes and sizes, and optical properties, such as optical depth, particle extinction and backscatter coefficients, of cirrus clouds to understand their impact on Earth's climate.

Lidar (LIght Detection And Ranging) is a well-established measurement technique for cirrus cloud investigations. A lidar system emits laser light pulses into the atmosphere. These pulses are transmitted through the atmosphere and are backscattered with different intensity at different altitudes from the illuminated atmospheric volume. The backscattered light contains information about the optical properties of the illuminated atmospheric volume. In case of a Rayleigh-Mie lidar, the wavelength of emitted light remains retained with elastic backscattering. This elastically backscattered light is recorded time-dependent. The altitude information can be calculated from the measured transit time of light and the known speed of light in air. In case of a Raman system, the inelastically backscattered light is additionally detected to the elastically backscattered light. The inelastically backscattered light on atmospheric molecules, for instance nitrogen molecules, differs in wavelength from the emitted light. This difference is large enough to separate the backscattered signals into inelastically molecular-backscattered signals and elastically particle-backscattered signals, with dichroic beam splitters for example. Based on that separation of backscattered light, it is possible to independently retrieve the extinction and backscatter coefficient. A high spectral resolution (HSR) lidar consists of a channel to detect elastically backscattered light and of a channel to discriminate between particle backscattered signals and molecular backscattered signals by taking advantage of their different Doppler broadened spectral distribution. The particle depolarization can be measured by emitting linear-polarized light into the atmosphere and detecting the fraction of backscattered light polarized perpendicular to the polarization plane of emitted light.

If the wavelength of the laser pulses is comparable to the size of scatterers, then the wavelength-dependent scattering behaviour can be used to investigate the micro-physical properties of these scatterers. As cirrus clouds contain ice crystals with sizes of several microns to some millimeters, this straightforward calculation is not applicable to determine their micro-physical properties out of lidar measurements.

Therefore, the optical properties particle depolarization ratio and particle lidar ratio are used in this study to investigate cirrus clouds. This approach bases on the independence of these optical intensive properties on particle mass. The particle depolarization ratio is the ratio of perpendicular- to parallel-polarized light backscattered from particles. The orientation of linear-polarized light is defined relative to the polarization plane of the emitted linear-polarized laser-light pulses.

The particle depolarization ratio contains the information whether the scattering particle is spherical or not. The transmission of the light pulses trough the atmosphere is related to the extinction of light by atmospheric molecules and particles. The particle lidar ratio is defined as the extinction-to-backscatter ratio of the particles. Just as the particle depolarization ratio, this ratio is also an optical intensive property of the scattering particles and depends mainly on their sizes and absorption properties.

Several studies on simultaneous measurements of particle depolarization ratios and particle lidar ratios of cirrus clouds differ in their findings and conclusions. While Chen et al. (2002) and Reichard et al. (2002) observed a correlation of the particle depolarization ratio with the particle lidar ratio of cirrus clouds, Sakai et al. (2006) reported a broad range of possible values and no clear correlation. Also, the impact of multiple scattering on retrieved particle lidar ratios is differently considered in these studies. All three authors discussed the possible micro-physical properties of ice crystals responsible for their observed optical parameters in a different manner. So, there is a lack of knowledge about the correlation of these optical properties and possibly their correlation with the micro-physical properties of cirrus clouds. This limits the applicability of lidar measurements for the retrieval of micro-physical properties of cirrus clouds.

The presented study investigates the correlation of the particle depolarization ratios with the particle lidar ratios of cirrus clouds over Leipzig, Germany. First, basics of the lidar data retrieval procedures are summarized in chapter 2. A literature study of so far measured particle depolarization ratios and particle lidar ratios of cirrus clouds is presented in chapter 3. Special emphasis is put on investigations dedicated to both of these intensive properties. Chapter 4 deals with the lidar system BERTHA (Backscatter, Extinction, lidar Ratio, Temperature, Humidity profiling Apparatus) and a first simultaneous measurement of these properties of cirrus clouds with BERTHA using its HSR channel is presented. For this measurement, the lidar system BERTHA was additionally equipped with a depolarization channel. Its usability for the determination of the particle depolarization ratio and particle lidar ratio at daytime is discussed. In this context, the receiver of the lidar system BERTHA was redesigned to provide multi-wavelength and multiple field-of-view (FOV) measurements on daytime and night-time. The measurement shows the advantages of the system BERTHA, but also presents needs of future improvements. In chapter 5, main parts of the lidar system Polly^{XT}, located on top of the roof of the Leibniz Institute for Tropospheric Research (TROPOS), are presented. An example measurement with Polly^{XT} is shown. After presenting the simultaneous measurements of particle depolarization ratios and particle lidar ratios of cirrus clouds, the chapter concludes with the measurement results. These measurements have been taken with the system Polly^{XT} between 30-07-2012 and 17-09-2012. The main findings are again outlined in the summary.

2 Lidar

Light detecting and ranging (lidar) is an active and range resolved optical remote sensing method. It is based on the same principle as radio detecting and ranging (radar). In contrast to passive optical remote sensing systems, which use extraneous light sources like ambient-light or sunlight, a laser pulse is emitted into the atmosphere and the backscattered light is detected by the lidar system.

Even though a laser light source was not invented, the acronym "lidar" was established by Middleton and Spilhaus (1953) when discussing ceilometry by using a spotlight. Initial lidar observations of the atmosphere with laser light were done by Fiocco and Smullin (1963) and Ligda (1963).

A lidar system consists of two main components: the transmitter and the receiver. On the transmitter side, a laser is used as a light source to emit light with specified pulse length and wavelength into the atmosphere. With additional optical systems, like beam expander and polarization filter, the laser divergence can be reduced and the state of polarization can be improved on the transmitter side. Due to elastic and inelastic scattering processes in the illuminated atmospheric volume the backscattered light contains information about this scattering volume. To obtain these information, the backscattered light is collected by a coaxial- or biaxial-arranged optical system at the receiver side (Harms and Weitkamp, 1978) and is directed into different detection channels. Depending on the lidar system type, the number and kind of these detection channels differ. Subsequently, the acquired input signals from these detection channels are stored and can then be evaluated. In the following, the evaluation of elastic and inelastic-backscattered light is presented for single-scattering processes at molecules and particles of the atmosphere.

2.1 Lidar measurement principle

The distance between the lidar system and the atmospheric scattering volume can be determined from the transit time of light t and the speed of light in air c to

$$R = \frac{c\,t}{2}\ . \tag{2.1}$$

The spatial depth of the atmospheric backscatter volume is related to the temporal laser pulse length τ and yields to

$$\Delta R = \frac{c\,\tau}{2}\ . \tag{2.2}$$

With regard to these two substitutions, the time dependent signal power of elastic and inelastic single-backscattered light, received at the lidar system can be with

$$P(R,\lambda_i) = K(\lambda_i)\,G(R)\,\beta(R,\lambda_i)\,T(R,\lambda_0)\,T(R,\lambda_i)\ . \tag{2.3}$$

The received lidar signal power depends on the system specific factor $K(\lambda_i)$, the backscatter coefficient $\beta(R,\lambda_i)$, the atmospheric transmission for emitted light $T(R,\lambda_0)$, the atmospheric transmission for backscattered light $T(R,\lambda_i)$ and the geometric factor $G(R)$ describing the geometrical signal-range dependence.

The following convention applies for this study. The index $i = 0$ is used for emitted light and for elastic-backscattered light, whereas the indices $i = \mathrm{Ra}$ and $i = \mathrm{HSRL}$ are used respectively in the context of Raman lidar and high spectral resolution lidar (HSRL) method.

System factor

All distance-independent parameter are contained in the system factor

$$K(\lambda_i) = P_0(\lambda_0)\,\Delta R\,A\,\eta(\lambda_i)\ . \tag{2.4}$$

The power of emitted light $P_0(\lambda_0)$ and the spatial effective pulse length ΔR are parameter of the emitter side. They affect the permeation and distance resolution

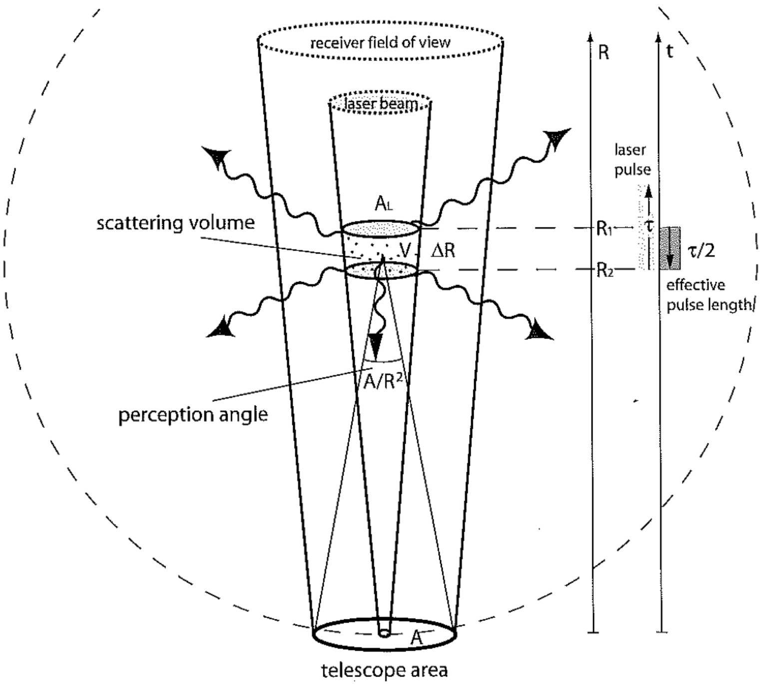

Figure 2.1: Illustration of the lidar geometry (Wandinger, 2005a).

of the emitted light. The telescope area A and the total system efficiency $\eta(\lambda_i)$ are parameter of the receiver side. They affect the signal power of light received by the telescope and by the photomultiplier detectors.

Geometric factor

For short distances from the scattering volume to the lidar system, the geometrical overlap between the laser beam and the telescope field of view (FOV) depends on the distance to the receiver. For long distances to the lidar system, the overlap between the laser beam and the telescope FOV achieves a constant value. Seen from the scattering volume perspective, the telescope area is a segment of a sphere's surface with radius R around the scattering volume. As shown in Fig. 2.1, the corresponding solid angle becomes A/R^2. Hence, the geometric factor consists of the system specific overlap function $O(R)$ and is reduced by $1/R^2$:

$$G(R) = \frac{O(R)}{R^2} \, . \tag{2.5}$$

Backscatter coefficient

The backscatter coefficient describes the fraction of light scattered back to the lidar system:

$$\beta(R,\lambda_i) = \sum_j n_j(R)\,\frac{d\sigma_{\text{sca},j}}{d\Omega}(\pi,\lambda_i) = \beta_{\text{mol}}(R,\lambda_i) + \beta_{\text{par}}(R,\lambda_i)\ . \tag{2.6}$$

It is the product of number density of the involved scatterer type j and the differential scattering cross section in backward direction ($\Theta = \pi$). The backscatter coefficient consists of the molecular backscatter coefficient and the particle backscatter coefficient. The molecular backscatter coefficient can be calculated analytically:

$$\beta_{\text{mol}}(R,\lambda_i) = n_i(R_0)\,\exp\left\{-\int\limits_{R_0}^{R} \frac{M\,g(r)}{R_\text{m}\,T_{\text{emp}}(r)}dr\right\}\frac{\pi^2(\tilde{n}_{\text{air}}^2-1)^2}{n_i(R)^2\,\lambda_i^4}\ . \tag{2.7}$$

The analytical calculation of the molecular backscatter coefficient is shown in appendix 7.1. The determination of the particle backscatter coefficient $\beta_{\text{par}}(R,\lambda_i)$ is explained in the following subchapters for elastic and inelastic-backscattered light.

Transmission

Light is attenuated due to absorption and scattering processes when it passes through the atmosphere. According to the Lambert-Beer-Bouguer law there is an exponential relation between the transmission and the extinction coefficient $\alpha(r,\lambda_i)$

$$T(R,\lambda_i) = \exp\left\{-\int\limits_{R_0}^{R}\alpha(r,\lambda_i)\,dr\right\}\ . \tag{2.8}$$

Extinction coefficient

The extinction coefficient is the product of the number density of the involved scatter types j and the extinction cross section $\sigma_{\text{ext},j}(\lambda_i) = \sigma_{\text{abs},j}(\lambda_i) + \sigma_{\text{sca},j}(\lambda_i)$

$$\alpha(R,\lambda_i) = \sum_j n_j(R)\,\sigma_{\text{ext},j}(\lambda_i) = \alpha_{\text{mol}}(R,\lambda_i) + \alpha_{\text{par}}(R,\lambda_i)\ . \tag{2.9}$$

Corresponding to the backscatter coefficient, the extinction coefficient consists of the molecular extinction coefficient, which can be calculated analytically

$$\alpha_{\text{mol}}(R,\lambda_i) = \frac{8\pi}{3} n_i(R_0) \exp\left\{ -\int\limits_{R_0}^{R} \frac{M\,g(r)}{R_{\text{m}}\,T_{\text{emp}}(r)} dr \right\} \frac{\pi^2(\tilde{n}_{air}^2 - 1)^2}{n_i(R)^2 \lambda_i^4} \;, \tag{2.10}$$

and the particle extinction coefficient $\alpha_{\text{par}}(R,\lambda_i)$. The analytical calculation of the molecular extinction coefficient is shown in appendix 7.1, and the determination of the particle extinction coefficient is shown in the following subchapters.

Lidar ratio

The ratio of extinction coefficient to backscatter coefficient is defined as lidar ratio for molecules and particles:

$$S_{\text{mol}} = \frac{\alpha_{\text{mol}}(R,\lambda_i)}{\beta_{\text{mol}}(R,\lambda_i)} = \frac{8\pi}{3} \tag{2.11}$$

and

$$S_{\text{par}}(R,\lambda_i) = \frac{\alpha_{\text{par}}(R,\lambda_i)}{\beta_{\text{par}}(R,\lambda_i)} \;. \tag{2.12}$$

The molecular lidar ratio is caused by Rayleigh-Brillouin scattering and can be calculated analytically whereas the particle lidar ratio cannot be calculated analytically for non-spheric particles.

2.2 Rayleigh-Mie lidar

The Rayleigh-Mie lidar is based on elastic backscattering on molecules and particles (Rayleigh-scattering, Mie-scattering respectively). As discussed in subchapter 2.2, an assumption of the lidar ratio profile is needed to determine the particle backscatter and extinction coefficient. Due to the large differential backscatter cross section for elastic scattering on molecules and particles, this lidar can be used to probe the atmosphere at day and nighttime.

Elastic-backscatter lidar equation

The wavelength of emitted light is conserved due to elastic scattering on molecules and particles. Hence, with $\lambda_i = \lambda_0$ Eq. 2.3 yields to

$$P(R, \lambda_0) = K(\lambda_0)\, G(R)\, \beta(R, \lambda_0)\, T^2(R, \lambda_0)\ . \tag{2.13}$$

This under-determined equation can not be solved without further assumptions. The Fernald-Klett method (Klett, 1981; Fernald, 1984) is commonly used in this case. Starting at a nearly particle free reference altitude R_0, a backward iteration yields to the particle backscatter coefficient profile $\beta_{\text{par}}(R, \lambda_0)$ by assuming the corresponding particle lidar ratio profile $S_{\text{par}}(R, \lambda_0)$ and the particle backscatter coefficient at the reference altitude $\beta_{\text{par}}(R_0, \lambda_0)$:

$$\begin{aligned}\beta_{\text{par}}(R, \lambda_0) = P(R, \lambda_0)\, R^2 \exp\left\{ -2 \int\limits_{R_0}^{R} [S_{\text{par}}(r, \lambda_0) - S_{\text{mol}}]\, \beta_{\text{mol}}(r, \lambda_0)\, dr \right\} \\ \times \left(\frac{P(R_0, \lambda_0)\, R_0^2}{\beta_{\text{par}}(R_0, \lambda_0) + \beta_{\text{mol}}(R_0, \lambda_0)} - 2 \int\limits_{R_0}^{R} S_{\text{par}}(r, \lambda_0)\, P(r, \lambda_0)\, r^2 \right. \\ \left. \times \exp\left\{ -2 \int\limits_{R_0}^{r} [S_{\text{par}}(s, \lambda_0) - S_{\text{mol}}]\, \beta_{\text{mol}}(s, \lambda_0)\, ds \right\} dr \right)^{-1} - \beta_{\text{mol}}(R, \lambda_0)\ .\end{aligned} \tag{2.14}$$

Hence, by using Eq. 2.12 the particle extinction coefficient can be obtained as

$$\alpha_{\text{par}}(R, \lambda_0) = S_{\text{par}}(R, \lambda_0)\, \beta_{\text{par}}(R, \lambda_0)\ . \tag{2.15}$$

The differential Eq. 2.13 can be solved in accordance to the Fernald-Klett method.

Linear depolarization of elastic-backscattered light

The polarization state of the received laser light with respect to the polarization state of the emitted laser light contains information about the particle shape. Herein after, the terms polarization and depolarization are used without explicitly stated "linear". The perpendicular-polarized light is detected in addition to the unpolarized elastic-backscattered light. Analogous to Eq. 2.13, the power of the perpendicular-polarized lidar signal is

$$P^{\perp}(R,\lambda_0) = K^{\perp}(\lambda_0) G(R)\, \beta^{\perp}(R,\lambda_0)\, T^2(R,\lambda_0)\ . \tag{2.16}$$

Compared to the system factor $K(\lambda_0)$ (Eq. 2.1) for elastic-backscattered light, the system factor $K^{\perp}(\lambda_0)$ depends on the system efficiency $\eta^{\perp}$ for perpendicular-polarized light:

$$K^{\perp}(\lambda_i) = P_0(\lambda_i)\, \Delta R\, A\, \eta^{\perp}(\lambda_i)\ . \tag{2.17}$$

The perpendicular component of the backscatter coefficient depends on the sphericity of the backscattering particles and the molecular depolarization characteristics:

$$\beta^{\perp}(R,\lambda_i) = \beta^{\perp}_{\text{mol}}(R,\lambda_i) + \beta^{\perp}_{\text{par}}(R,\lambda_i)\ . \tag{2.18}$$

The ratio of the elastic-backscattered perpendicular- and parallel-polarized laser light is defined as volume depolarization ratio:

$$\delta_{\text{vol}}(R,\lambda_i) = \frac{\beta^{\perp}(R,\lambda_i)}{\beta^{\|}(R,\lambda_i)} = \frac{\beta^{\perp}_{\text{mol}}(R,\lambda_i) + \beta^{\perp}_{\text{par}}(R,\lambda_i)}{\beta^{\|}_{\text{mol}}(R,\lambda_i) + \beta^{\|}_{\text{par}}(R,\lambda_i)}\ . \tag{2.19}$$

Analogously, the molecular and particle depolarization ratio are defined as

$$\delta_{\text{mol}}(R,\lambda_i) = \frac{\beta^{\perp}_{\text{mol}}(R,\lambda_i)}{\beta^{\|}_{\text{mol}}(R,\lambda_i)} \tag{2.20}$$

and

$$\delta_{\text{par}}(R,\lambda_i) = \frac{\beta^{\perp}_{\text{par}}(R,\lambda_i)}{\beta^{\|}_{\text{par}}(R,\lambda_i)}\ . \tag{2.21}$$

The volume and particle depolarization ratio can by determined with the depolarization lidar method (Murayama et al. (1999), Cairo et al. (1999) and Freudenthaler et al. (2009)) by using Eq. 2.13 and Eq. 2.16. Instead of measuring the parallel- and perpendicular-polarized backscattered light, the lidar systems Polly^{XT} and BERTHA measure the elastic-backscattered and perpendicular-polarized light. Thus, according to Baars (2012), the volume depolarization ratio can be retrieved out of the perpendicular-polarized and elastic-backscattered light by

$$\delta_{\text{vol}}(R,\lambda_i) = \frac{C^{\delta}_{\lambda_i} - \frac{P^{\perp}(R,\lambda_i)}{P(R,\lambda_i)}}{D_{\lambda_i}\frac{P^{\perp}(R,\lambda_i)}{P(R,\lambda_i)} - D^{\perp}_{\lambda_i}\,C^{\delta}_{\lambda_i}}\ . \tag{2.22}$$

The calibration constant $C^{\delta}_{\lambda_0}$, which is determined in a particle free atmospheric region after Grein (2006) and the received perpendicular-polarized and elastic-backscattered signals $P^{\perp}(z,\lambda_0)$ and $P(z,\lambda_0)$ are taken from the depolarization channel and the total channel, respectively. The transmission ratio for perpendicular- and parallel-polarized light ($D^{\perp}_{\lambda_0}$, D_{λ_0}) are determined experimentally for the depolarization channel and total channel respectively. Hence, the particle depolarization ratio can be determined, according to Mattis (2002), by using the particle and molecular backscatter coefficient:

$$\delta_{\text{par}}(R,\lambda_i) = [\delta_{\text{vol}}(R,\lambda_i)+1]\left(\frac{\beta_{\text{mol}}(R,\lambda_i)[\delta_{\text{mol}}(R,\lambda_i)-\delta_{\text{vol}}(R,\lambda_i)]}{\beta_{\text{par}}(R,\lambda_i)[1+\delta_{\text{mol}}(R,\lambda_i)]}+1\right)^{-1} - 1\ . \tag{2.23}$$

2.3 Raman lidar and High spectral resolution lidar

As discussed in subchapter 2.3, the particle backscatter and extinction coefficient can be determined separately by using the elastic and inelastic-backscatter signal. According to this, a Raman lidar is always a Rayleigh-Mie lidar, too. The detected light at the wavelength λ_{Ra} is exclusively based on Raman scattering on the corresponding type of molecule. For example, the wavelength of the vibration-rotation Raman signal of nitrogen is $\lambda_{Ra} = 607\,\text{nm}$ ($\lambda_0 = 532\,\text{nm}$). Due to the low differential backscatter cross section for Raman scattering on molecules, the Raman lidar is affected negatively on ambient-light and thus only partially usable on daytime.

While the Raman lidar is based on vibrational-rotational transitions of molecules, the HSRL is based on the Doppler broadening of the backscattered light due to the

Brownian motion of molecules. The molecular mean velocity $\approx 300\,\mathrm{m/s}$ yields to a broadening of $\pm 1.5\,\mathrm{GHz}$ (FWHM) whereas the particle mean velocity $\approx 10\,\mathrm{m/s}$ yields to a broadening of only $30\,\mathrm{MHz}$ (FWHM). To separate the backscattered molecular signal from the particle signal, a very narrow optical filter is needed these can be e.g. a Fabry-Perot interferometer or absorption line filter. As described in the following an iodine-vapour cell is used for this study. The corresponding HSR channel is discussed in the master thesis of Oelsner (2012). In contrast to the Raman lidar, the HSRL can be used on daytime due to the high differential backscatter cross section of scattering on molecules (analogical to the Rayleigh-Mie lidar).

Inelastic-backscatter lidar equation

For inelastic scattering, the wavelength of backscattered light differs from the emitted light wavelength and thus Eq. 2.3 yields to

$$P_{\mathrm{Ra}}(R,\lambda_{\mathrm{Ra}}) = K(\lambda_{\mathrm{Ra}})\,G(R)\,\beta(R,\lambda_{\mathrm{Ra}})\,T(R,\lambda_0)\,T(R,\lambda_{\mathrm{Ra}})\;. \tag{2.24}$$

The Raman lidar method and the HSRL method are both based on inelastic backscattering of the emitted light. Although the index $i = \mathrm{Ra}$ is used, the given equations apply to the Raman lidar method as well as to the HSRL method.

As the number density of the corresponding molecules $n_{\mathrm{Ra}}(R)$ are known, according to Ansmann et al. (1990) the particle backscatter coefficient can be determined as

$$\beta_{\mathrm{par}}(R,\lambda_0) = \beta(R_0,\lambda_0)\frac{P_{\mathrm{Ra}}(R_0,\lambda_{\mathrm{Ra}})}{P_{\mathrm{Ra}}(R,\lambda_{\mathrm{Ra}})}\frac{P(R,\lambda_0)}{P(R_0,\lambda_0)}\frac{n_{\mathrm{Ra}}(R)}{n_{\mathrm{Ra}}(R_0)}\frac{\exp\left\{-\int\limits_{R_0}^{R}\alpha(r,\lambda_{\mathrm{Ra}})\,dr\right\}}{\exp\left\{-\int\limits_{R_0}^{R}\alpha(r,\lambda_0)\,dr\right\}} - \beta_{\mathrm{mol}}(R,\lambda_0)\;. \tag{2.25}$$

This solution is based on the elastic-backscatter lidar signal $P(R,\lambda_0)$ and the inelastic-backscatter lidar signal $P_{\mathrm{Ra}}(R,\lambda_{\mathrm{Ra}})$. As a result, the Eq. 2.13 and Eq.

2.24 are a well-determined system and thus the particle backscatter coefficient $\beta_{\text{par}}(R, \lambda_0)$ and the particle extinction coefficient $\alpha_{\text{par}}(R, \lambda_0)$ can be determined without any assumptions

$$\alpha_{\text{par}}(R, \lambda_0) = \frac{\frac{d}{dR} \ln \frac{n_{\text{Ra}}(R)\, G(R)}{P_{\text{Ra}}(R, \lambda_{\text{Ra}})} - \alpha_{\text{mol}}(R, \lambda_0) - \alpha_{\text{mol}}(R, \lambda_{\text{Ra}})}{1 + \left(\frac{\lambda_0}{\lambda_{\text{Ra}}}\right)^a} \; . \tag{2.26}$$

The spectral dependence of particle scattering is described by the Ångstöm exponent a (Ångstöm, 1964; Ansmann and Müller, 2005). For particles within the size range of the emitted light wavelength, the Ångstöm exponent can be assumed to $a = 1$ and for particles larger than the emitted light wavelength, e.g. ice crystals, the Ångstöm exponent becomes $a = 0$ (van de Hulst, 1981). According to Ansmann et al. (1992), an uncertainty of $\Delta a = \pm 0.5$ leads to a particle extinction coefficient uncertainty of 2%.

3 Cirrus clouds

This chapter gives an overview of the interrelation between ice crystals contained in cirrus clouds and their optical properties. For this purpose, the definition of cirrus clouds used in this study is presented. The impact of cirrus clouds on climate and resulting questions is mentioned briefly. Cirrus clouds affect the radiative balance in two ways. Depending on size and structure of the contained ice crystals, cirrus clouds reflect solar radiation (albedo effect) and terrestrial radiation (green house effect) in a different manner. Hence, the growth of ice crystals from vapour plays an important role. First assumptions about size and ice-crystal type can be made out of occurring optical phenomena. But their infrequent occurrence indicate a distribution of different crystal types and sizes and thus do not provide long-term explorations.

The intensive optical properties particle depolarization ratio and particle lidar ratio provide the determination of crystal type and the assumption of crystal size. But the underestimation of the extinction coefficient due to multiple scattering requires additional corrections.

After former measurements and resultant conclusions have been presented, this chapter concludes with an overview of measured and calculated values of particle depolarization ratio and particle lidar ratio.

3.1 What is a cirrus cloud

Clouds are classified by a nomenclature system, whose essentials were proposed in 1802 by Luke Howard. Nowadays, the World Meteorological Organization (WMO) is responsible for this classification system. In accordance to the WMO classification system, clouds of the genus cirrus belong to the family of high clouds. Hence, they are familiar with clouds of the genus cirrostratus and cirrocumulus. High clouds are defined by the WMO classification system as transparent, thin white, or mostly white clouds with a fibrous or smooth appearance, silky sheen, or without shading. This classification system is primarily based on the morphology and visual appearance of clouds during daytime and does not contain information about the physical properties. As cloud properties like ice content, temperature, humidity, ventilation, altitude, and optical depth are not part of the classification system, it is limited in its applicability for this study. For these reasons, a further reaching definition of cirrus clouds shall be used in this study:

Cirrus clouds are completely composed of ice, have a usually mean cloud base altitude of $6\,\mathrm{km}$ or higher and a small optical depth.

This definition not only includes cirrus, cirrostratus and cirrocumulus clouds but also subvisual cirrus and contrail cirrus clouds, which was not mentioned by the WMO classification system before.

3.2 Effects on climate

A crucial part of the weather system plays the amount and distribution of solar radiation received and reflected by Earth and its atmosphere.

Cirrus clouds are composed of ice crystals, occur in the upper troposphere and they affect the radiation balance in two ways. For outgoing terrestrial radiation in the infrared region they act like a blanket and protect the Earth from cooling down (greenhouse effect). For example, beneath a cirrus cloud the air temperature raises by $10\,^{\circ}\mathrm{C}$. In the same way they reflect the incoming solar radiation back to space and prevent the Earth from overheating (albedo effect). The net impact of cirrus clouds on our climate system is determined by the balance between these two radiative processes.

Stephens et al. (1990) showed that their scattering calculations reasonably matched to lidar and radiometer data by assuming a particle size of $r_e = 16\,\mu\mathrm{m}$. But, by comparing cloud radiation properties measured from aircraft to their parametrized cloud radiation properties, they derived significantly smaller asymmetry parameters g than those for spheres. Their climate simulation revealed that the influence of cirrus clouds on climate was strongly affected by the hardly known parameters r_e and g. Additionally, they showed that the assumed value of r_e could either enhance or reduce the effect of ice water feedback on a CO_2 warming simulation.

The formation of cirrus clouds depends on water vapour content, temperature, and atmospheric pressure in the associated altitude. By undergoing deposition, water vapour develops ice crystals. This process can be observed, for instance, in the outflow of cyclones or in the anvil of cumulonimbus clouds. The micro-physical and macro-physical properties like size distribution, asymmetry parameter and shape vary depending on the cirrus cloud generating weather process. These processes in turn depend on geographic location.

To conclude, cirrus cloud properties are a function of water vapour content, temperature, atmospheric pressure, generation process and thus also geographic location. Consequently, the radiative properties of cirrus clouds over the arctic differ from those over middle latitudes and the tropics. Although, cirrus clouds are the object of research for decades and their nature and interaction with the local weather system is well known the impact of cirrus clouds on the global weather system is yet to be investigated.

The motivation of this study can be summarized in three questions.

- How will cirrus clouds respond or feedback to global warming effects?
- Could cirrus clouds reinforce or negate the theoretically predicted global warming?
- Do aircraft traffic and agricultural activities increase the ice-crystal concentration in the upper troposphere and thus creating more cirrus cloud cover in a radiatively important sense?

To answer these questions it is necessary to continuously measure cirrus cloud properties at as many locations as possible. Lidar is one range-resolved technique able to measure the basal optical properties. Temperature, humidity and state of matter can be derived from lidar data since many years.

3.3 The growth of ice crystals

The habits of ice crystals grown from the vapour exhibit a large variety of shape and size. When ice crystals grew from vapour, its water molecules are aligned in a hexagonal crystal lattice structure. According to Nakaya (1954), the shape and size of an ice particle depends closely on the temperature and the excess vapour density relative to ice of the environment. This classification of growth morphology has been extended by Hallett and Mason (1958) and by Kobayashi (1961). As seen in Fig. 3.1, for a low excess vapour density and thus a low growth rate simple crystal shapes are formed while at higher excess vapour density and thus faster growth rates the crystal habit becomes more intricate. The shape varies from thin plates over hollow columns to long needles. In the temperature region of $0\,^{\circ}$C to $-3\,^{\circ}$C and $-10\,^{\circ}$C to $-20\,^{\circ}$C plate like crystals are formed. While between $-3\,^{\circ}$C and $-10\,^{\circ}$C and below $-22\,^{\circ}$C column like crystals dominate. The complex growth process is aggravated by collisions forming extremely complex crystal shapes. In-situ measurements in cirrus clouds confirm this thesis. All ice crystals grown from vapour (shown in

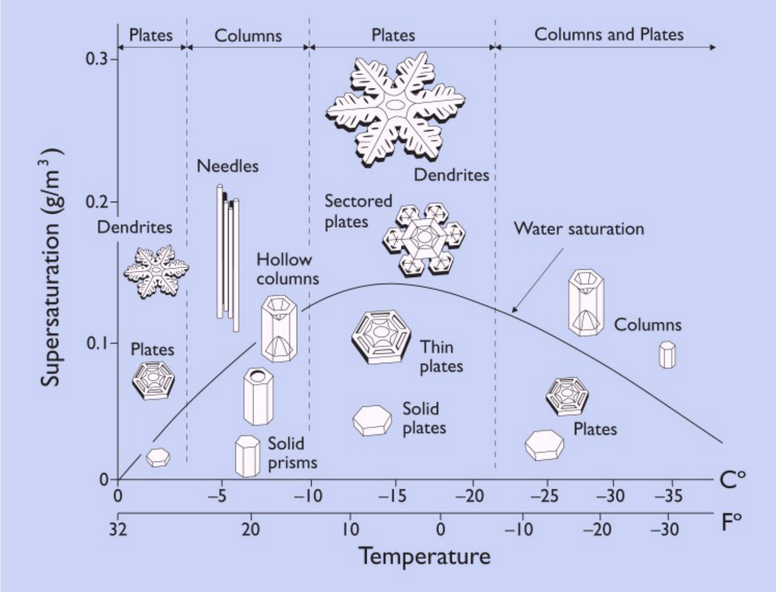

Figure 3.1: Nakaya - Kobayashi diagram, illustrating the morphology of ice crystals as a function of supersaturation and temperature (Libbrecht, 2001).

Fig. 3.1) can be found in cirrus clouds as well as crystals with high irregular surfaces formed by collisions, with sizes of a few microns to thousands of microns and in any composition of shape and size.

3.4 Optical phenomena and resultant properties

First assumptions about the micro-physical properties of cirrus clouds can be made of distinctive optical phenomena. Cirrus clouds produce optical effects like glories, halos, parhelia as well as circumzenithal and circumhorizontal arcs. Although these effects are not always obvious, they can be seen anywhere in the world and at any season.

A glory consists of concentric colored rings appearing around the shadow of the observer, the anti-solar point. Glories are attributed to water droplets although they are also rarely observed formed by cirrus clouds. According to Sassen et al. (1998), the ice-crystal shape must be near spherical with a diameter of $9 - 15\,\mu\text{m}$.

A parhelion is a bright spot of light in the sky on either side of the Sun. They appear at 22° azimut to the Sun and at the same height above the horizon as the Sun. They are commonly made of plate shaped hexagonal ice crystals. They bend the light rays by passing through them with a minimum deflection angle of 22°. When plate shaped ice crystals sink through the air they become vertically aligned. Hence, the sunlight is refracted horizontally and parhelia can be observed. A complete 22° ring, or halo, appears if the ice crystals are randomly oriented.

The circumzenithal and circumhorizontal arcs are formed by plate shaped and vertically aligned ice crystals. At 46° underneath the Sun, the circumhorizontal arc appears as a multi-coloured band running parallel to the horizon. This phenomenon is formed by sunlight entering a vertical side face of a plate shaped ice crystal and leaving through the horizontal bottom face.

The circumzenithal arc is an optical phenomenon similar to the circumhorizontal arc, but it is formed by sunlight entering the horizontal side face of a plate shaped ice crystal and leaving through a vertical side face. Hence, this phenomenon appears only on the same side as the Sun. Not more than one quarter of a zenith centered circle above the Sun is formed.

When optical phenomena appear, they indicate a pure state of particle shape, size distribution and orientation. But their infrequent presence shows that the required observation conditions are to rarely fulfilled and the situation is more complex.

3.5 Single scattering on ice crystals

Whereas scattering on molecules and spheric particles can be analytically calculated due to the hexagonal crystal structure of ice, the scattering on ice crystals is more complex. Hereby the size and shape of ice particles in cirrus clouds varies from $10\,\mu\mathrm{m}$ to $1\,\mathrm{mm}$ and from regular shaped plates and columns to complex structures of hexagonal prisms and sectored dendrites.

According to Wandinger (1994), the Mueller calculus for randomly distributed hexagonal ice crystals, having a plane of symmetry, yields to

$$\begin{pmatrix} I_\mathrm{s} \\ Q_\mathrm{s} \\ U_\mathrm{s} \\ V_\mathrm{s} \end{pmatrix} = \frac{\sigma_\mathrm{sca}}{r^2} \begin{pmatrix} P_{11} & P_{12} & 0 & 0 \\ P_{12} & P_{22} & 0 & 0 \\ 0 & 0 & P_{33} & P_{34} \\ 0 & 0 & -P_{34} & P_{44} \end{pmatrix} \begin{pmatrix} I_\mathrm{e} \\ Q_\mathrm{e} \\ U_\mathrm{e} \\ V_\mathrm{e} \end{pmatrix} . \tag{3.1}$$

The Stokes vector of scattered light (index s) depends on the radial distance to the scattering centre r, the scattering cross section σ_sca and the matrix product of the scattering phase matrix and the Stokes vector of emitted light (index e). In the case of exact backscattering, the matrix elements P_{12}, P_{34} are zero and thus the scattering phase matrix becomes diagonal for a scattering angle $\Theta = \pi$. As the equation above shows, the matrix elements P_{11}, P_{12} impact on the particle backscatter coefficient and particle extinction coefficient and the matrix elements P_{11}, P_{12}, P_{22} yield to the particle depolarization ratio

$$\delta_\mathrm{par}(R, \lambda_i) = \frac{(P_{11} + P_{12}) - (P_{12} + P_{22})}{(P_{11} + P_{12}) + (P_{12} + P_{22})} = \frac{I_\mathrm{s} - Q_\mathrm{s}}{I_\mathrm{s} + Q_\mathrm{s}} . \tag{3.2}$$

Thus, the intensive properties $S_\mathrm{par}(R, \lambda_i)$ and $\delta_\mathrm{par}(R, \lambda_i)$ can be used as an indicator of the present ice-crystal type.

3.6 Multiple scattering on ice crystals

All previously discussed equations are valid only for single-backscattered lidar signals. But this assumption is incorrect for cirrus clouds. The degree of multiple-scattering influence on the lidar signal depends on the FOV, the distance to the scattering volume, the ice-crystal type and the ice-crystal size. Up to 50% of the scattered light is scattered into forward direction in the case of ice crystals (Wandinger, 1994). Hence, a fraction of non-backscattered light remains in the FOV. The influence of multiple scattering on the retrieved lidar signal can be calculated with knowledge of the effective particle size r_e and particle type. As discussed in subchapter 4.5, the particle size of ice crystals can be determined with the HSR channel in combination with a multiple-FOV setup. But this method was not available for this study, therefore all presented signals are not multiple-scattering corrected. Thus, the presented data (subchapter 5.4) is comparable with Chen et al. (2002) and Sakai et al. (2006) and discussed in the next chapter. As a result, the particle lidar ratio might be underestimated compared to its true value because the forward scattered light reduces the retrieved extinction coefficient. According to Wandinger (1998), Reichard et al. (2000) and Sakai et al. (2003) this underestimation can be up to 50%.

In contrast, double-scattering calculations revealed no significant difference between the particle depolarization ratio of cirrus clouds for single- and double-scattered light (Wandinger, 1994).

3.7 Contradictory findings from previous measurements and simulations of particle depolarization ratio and particle lidar ratio of cirrus clouds

Different positions about the combined measurement of particle depolarization and particle lidar ratio are introduced in this subchapter. Especially the question if it is possible or not to infer micro-physical properties from the application of particle depolarization and particle lidar ratio has to be investigated more thoroughly. A comparison and overview of relevant papers is discussed in the following. The emphasis is on papers about particle depolarization ratio and particle lidar ratio.

3.7.1 Particle depolarization and particle lidar ratio detected by lidar

Lidar measurements are used to investigate cirrus cloud properties since several decades. This research is based on the sensitivity of the particle extinction-to-backscatter ratio, also called particle lidar ratio and particle depolarization ratio.

Micro-physical properties of ice crystals like size distribution and refractive index affect the particle lidar ratio. Furthermore, the shape as well as the aspect ratio of ice crystals influences the particle depolarization ratio. In several papers it is discussed whether it is possible to retrieve these micro-physical properties or parts of them by measuring the particle depolarization and particle lidar ratio remotely.

The paper of Chen et al. (2002) and Guasta (2001) are representative for two different opinions. Chen et al. (2002) used a lidar system located at Chung-Li, Taiwan to study the particle lidar and particle depolarization ratios for cirrus clouds. Contrary to this, Guasta (2001) used a simulation code, called "face-tracing", that is derived from ray tracing. By this Guasta (2001) computed the particle lidar and particle depolarization ratios of cirrus clouds.

According to the statement of Chen et al. (2002) it is possible to retrieve various forms of hexagonal crystals by using the particle lidar and particle depolarization ratios.

Controversial to this statement, Guasta (2001) reported that it would theoretically be possible to joint estimate the size and aspect ratio of populations of randomly oriented isomorphic pristine crystals by comparing the experimental data of particle lidar and particle depolarization ratios with simulated ones. But in a mixture of pristine crystals with different aspect ratios, compact particles have a larger backscatter efficiency than plates or columns with the same total surface. Consequently, the presence of compact particles dominate the particle lidar and particle depolarization ratios regardless of a high incidence of deformed hexagonal crystals. According to Guasta (2001), in this mixture the particle lidar and particle depolarization ratios can only be used for a rough estimation of the ice-crystal size through the size dependency of the particle lidar ratio. In this context Guasta (2001) affirms that the particle lidar and particle depolarization ratios are insensitive indicators of the micro-physical properties of high cirrus clouds when compact pristine ice crystals are present.

To summarize, the determination of micro-physical properties of ice crystals in cirrus clouds, as for instance shape, aspect ratio and size distribution, appears plausible by evaluating particle lidar and particle depolarization ratios. Possible effects like from compact pristine ice crystals must be considered in the retrieval algorithm.

3.7.2 Relation between particle depolarization ratio and particle lidar ratio

The reflection and absorption of particles in mid- to high-level clouds critically depend on the phase and orientation (Asano, 1983; Liou, 1986). It is therefore necessary to determine the phase and orientation of those particles. The relation between the particle depolarization and particle lidar ratio of cirrus clouds are contradictory reported by Reichard et al. (2002) (Fig. 3.3) and Chen et al. (2002) (Fig. 3.4). Both reported that the plot of particle depolarization versus particle lidar ratio splits into two branches, but they measured different correlations. In Reichard et al. (2002) a strong positive correlation of particle depolarization ratio with particle lidar ratio for $\delta \lesssim 40\,\%$ and an anti-correlation for $\delta \gtrsim 40\,\%$ is yielded (Fig. 3.3). Compared to this Chen et al. (2002) reported that the particle depolarization ratio splits into two branches for $S > 30\,\mathrm{sr}$: one branch with high particle depolarization ratio $\delta \sim 50\,\%$ and the other one with $\delta \sim 20\,\%$ (Fig. 3.4). However, the reported curve progression is antipodal to the results of Reichard et al. (2002). According to Chen et al. (2002), the difference of the particle depolarization ratios of the two branches increases by increasing particle lidar ratio values. In contrast, Reichard et al. (2002) reported that this difference decreases by increasing particle lidar ratio values.

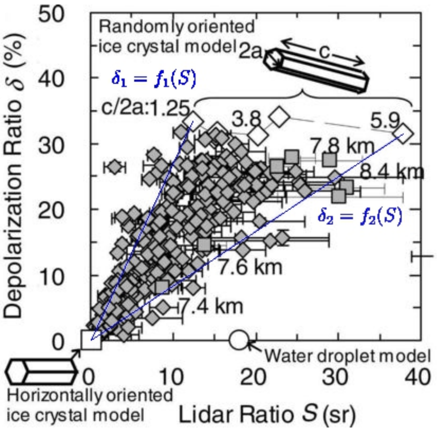

Figure 3.2: Sakai et al. (2006), details see below.

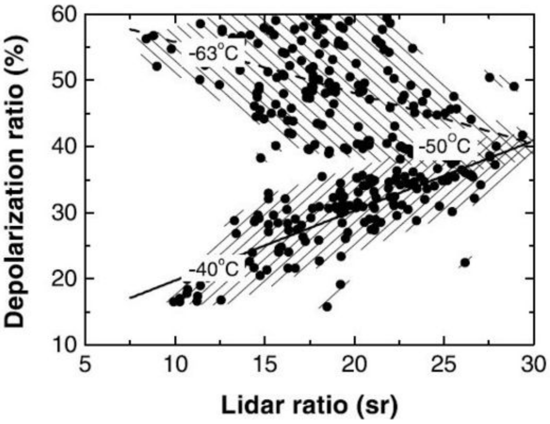

Figure 3.3: Reichard et al. (2002), details see below.

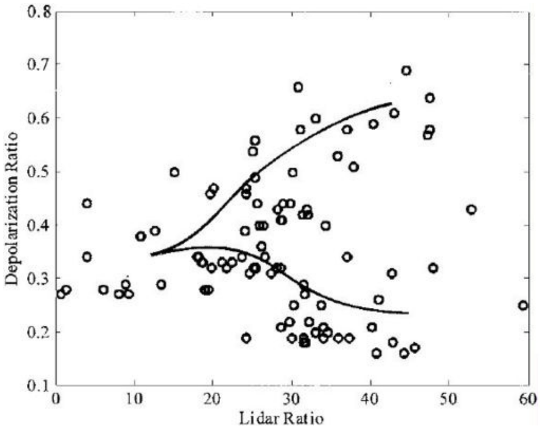

Figure 3.4: Chen et al. (2002), details see below.

Correlation of particle depolarization with particle lidar ratio at $532\,\mathrm{nm}$ wavelength (Fig. 3.2), $355\,\mathrm{nm}$ wavelength (Fig. 3.3) and $532\,\mathrm{nm}$ wavelength (Fig. 3.4). The vertices δ_1 and δ_2 in Fig. 3.2 were included for the discussion.

Unaffected by the latter statements, Sakai et al. (2006) reported that most of the measured particle depolarization and particle lidar ratio values are within an area enclosed by two vertices $\delta_1 = f_1(S)$ and $\delta_2 = f_2(S)$ (Fig. 3.2). These two vertices represent the theoretical values for randomly oriented ice crystals. The upper vertex $\delta_1 = f_1(S)$ represents randomly oriented ice crystals with an aspect ratio of $\frac{c}{2a} = 1.25$ and the lower vertex $\delta_2 = f_2(S)$ represents randomly oriented ice crystals with an aspect ratio of $\frac{c}{2a} = 5.9$.

Sakai et al. (2006) used a lidar system with a laser at $\lambda = 532\,\mathrm{nm}$ wavelength and $2\,\mathrm{mrad}$ field of view of the receiver to measure the micro-physical properties of upper clouds at an altitude range of $5 - 11\,\mathrm{km}$ over Tsukuba, Japan. Chen et al. (2002) used a lidar system with a laser at $\lambda = 532\,\mathrm{nm}$ wavelength to probe cirrus clouds over Chung-Li, Taiwan. Reichard et al. (2002) used a two-wavelength polarization Raman DIAL to probe cirrus clouds over Esrange, Sweden. The wavelengths of the emitted laser light were $\lambda = 308\,\mathrm{nm}$ and $\lambda = 355\,\mathrm{nm}$. The discussed values are measured at $\lambda = 355\,\mathrm{nm}$ wavelength. So the discrepancy might be due to the used wavelength or due to different cirrus particles that were observed.

To summarize, three different statements about the correlation of the particle depolarization with the particle lidar ratio of particles in cirrus clouds were introduced. First, the particle depolarization ratio splits into two branches. With increasing particle lidar ratio values, the difference of these two branches decreases (Reichard et al., 2002). Second, the particle depolarization ratio splits into two branches. But with increasing particle lidar ratio values, the difference of these two branches increases (Chen et al., 2002). Third, most of the values for particle depolarization and particle lidar ratio are enclosed between two vertices witch represents randomly oriented ice crystals with an aspect ratio of $\frac{c}{2a} = 1.25$ and $\frac{c}{2a} = 5.9$ respectively (Sakai et al., 2006). It might be possible to distinguish the phase and orientation of randomly oriented ice crystals by measuring the particle depolarization and particle lidar ratio (Sakai et al., 2006).

4 Lidar system BERTHA

The multi-wavelength depolarization Raman lidar BERTHA (Backscatter, Extinction, lidar Ratio, Temperature Humidity Apparatus) is a container-based system (Fig. 4.2) and described by Althausen et al. (2000). Parts of this system were used to build a HSRL (Oelsner, 2012). These parts were in particular the wavelength stabilised Nd:YAG laser, the Cassegrain receiver telescope, the Raman channel at 607 nm wavelength, and the total channel at 532 nm wavelength.

Based on this, a new lidar system was designed to measure profiles of the particle depolarization ratio at three wavelengths (355 nm, 532 nm, 1064 nm), the particle extinction coefficient at three wavelengths (387 nm, 532 nm, 607 nm), the water vapour mixing ratio, and the tropospheric temperature profile.

On that basis, a depolarization channel was added to the lidar system BERTHA in course of this study. The depolarization channel was characterised and its transmission ratio determined. An occurring cross talk in the HSR channel was examined and explained on the base of a non negligible relaxation time of excited states of Iodine vapour in the cell. After the measurement of cirrus clouds on 31-07-2012 has been presented this chapter closes with an outlook on the complete lidar system BERTHA.

4.1 Lidar system BERTHA

With the added depolarization channel the lidar system BERTHA is able to measures the depolarized signal at 532 nm wavelength, the Raman backscattered intensity from Nitrogen molecules at 607 nm wavelength, and the Rayleigh-Brillouin scattering signal at 532 nm wavelength. Therefore a depolarization channel was added to the existing HSRL system.

The general setup of the lidar system is shown in Fig. 4.1. Laser pulses at 1064 nm wavelength with 1.6 J/pulse are generated by a seeded Nd:YAG laser (Continuum, Powerlite 9030; Fig. 4.1, 1). After this laser, a second harmonic generation crystal is used to generate pulses at 532 nm wavelength having an energy of 600 mJ/pulse. The beam separator (Fig. 4.1, 6) reflects the light with 532 nm wavelength and transmits the radiation with 1064 nm wavelength which is dumped by the element (7). Hence, only pulses with 532 nm wavelength are emitted into the atmosphere. The wavenumber of the emitted light is monitored with a wavemeter (TOPTICA Photonics AG, WSU/30; Fig. 4.1, 3). This wavemeter is periodically calibrated with a continuous-wave HeNe laser (632.9914 nm in air, accuracy of ±0.0003 nm; Fig. 4.1, 4). By this, the seeder can be controlled and tuned to the wavenumber of the iodine absorption line #1109 by adjusting the seeder voltage setting (Fig. 4.1, 2). The generated light pulses are transmitted through expansion and steering optics (Fig. 4.1, 8, 9) and deflected by a deflecting-mirror at an zenith angle of 5° into the atmosphere.

At the receiver side, a deflecting-mirror reflects the backscattered light to the Cassegrain telescope (Fig. 4.3). Its parabolic primary mirror (Fig. 4.3, 1) has a diameter of 530 mm, the effective focal length of the telescope is 2973 mm. The aperture of 2.4 mm (Fig. 4.3, 4) yields to a FOV of 0.8 mrad. An off-axis parabolic mirror (Fig. 4.3, 5) collimates the backscattered light, reflects it into the optical setup with the camera to control the overlap and with the four detection channels.

The vibrational-rotational Stokes-Raman backscattered light by Nitrogen molecules has a central wavelength of 607.3 nm. It is detected by the Raman channel that consists of neutral density filters, an interference filter with a central wavelength of 607.3 nm and a FWHM of 3 nm, a focusing lens, and the PMT detectors.

The HSR channel consists of neutral density filters, the iodine-vapour cell, lenses to guide the light through the cell and to focus it onto the photomultiplier detector. The

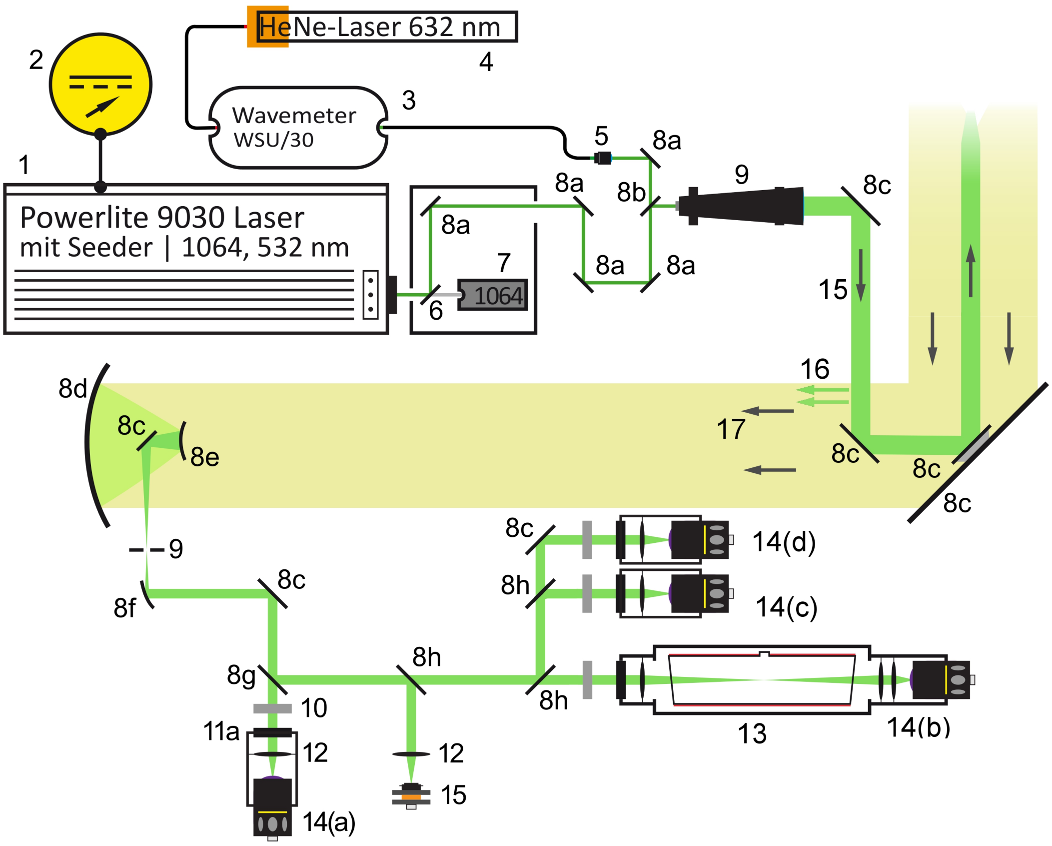

Figure 4.1: Configuration of BERTHA with its emitter and receiver (adopted from Oelsner (2012) and modified).

1	Continuum Powerlite 9030 Laser (Nd: YAG, 1064 nm and doubled to 532 nm)
2	Seeder voltage setting to adjust the seeder within a range of ±10 GHz
3	Wavemeter to control the laser pulse wavelength
4	Reference laser (HeNe, 632.9914 nm in air, accuracy of ±1 MHz)
5	Collimator
6	Dichroic beam splitter (high transmittance at 1064 nm, high reflectance at 532 nm)
7	Beam dump for laser pulses at 1064 nm wavelength
8a	Mirror (532 nm)
8b	Mirror (532 nm, polished backside, transmission $< 1‰$)
8c	Mirror (532 nm, metal coated)
8d	Parabolic primary Mirror
8e	Hyperbolic secondary Mirror
8f	Off-axis parabolic Mirror
8g	Dichroic beam splitter (high transmittance at 607 nm, high reflectance at 532 nm)
8h	Non-polarizing plate beam splitter for the wavelength 532 nm (50/50)
9	Aperture (2.4 mm diameter)
10	Neutral density filter
11a	Interference filter (607.3 nm)
11b	Interference filter (532.075 nm)
12	Lenses
13	Iodine-vapour cell with housing for temperature control
14	Photomultiplier
14a	Detector for Raman channel
14b	Detector for HSR channel
14c	Detector for depolarization channel (532 nm)
14d	Detector for total channel (532 nm)
15	Emitted laser pulse
16	Stray radiation
17	Backscattered light

Figure 4.2: Container housing of BERTHA. The deflecting-mirror to deflect the laser pulse into the atmosphere and reflect the incident light to the telescope can be seen on the front right side of the picture (made by D. Althausen).

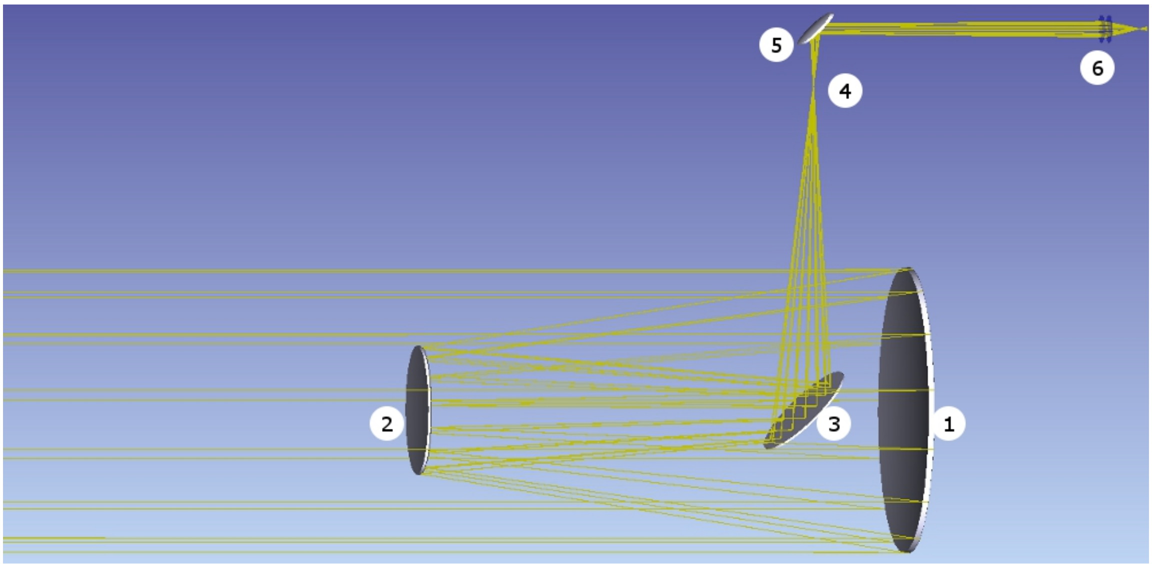

Figure 4.3: The Cassegrain telescope of BERTHA's receiver. 1: Parabolic primary mirror, 2: Hyperbolic secondary mirror, 3: Deflecting-mirror, 4: Aperture, 5: Off-axis parabolic mirror, 6: Focusing lenses and detector. Simulated with Zemax (Zemax Development Corporation, 2010).

illuminated volume inside the iodine-vapour cell has a double cone shape to ensure no shading and reflection effects. To suppress possible fluorescence radiation, an interference filter with 532.075 nm central wavelength and 1 nm FWHM is installed after the iodine-vapour cell.

The Raman channel and HSR channel measure only the backscattered light in a narrow range of wavelength. Whereas the total channel measures as well backscattered light from particles (Mie-scattering) as from molecules (Rayleigh-scattering) at 532 nm wavelength. Also the total channel consists of neutral density filters, an interference filter with 1 nm FWHM, and a lens to focus the light onto the PMT detector.

Those three channels measure the backscattered light regardless of the polarization state of light. A depolarization channel is added to BERTHA to measure the linear depolarization of backscattered light. The configuration of this channel is the same as for the total channel except of the additional integrated polarization filter that is rotated perpendicular to the polarization direction of the emitted laser light.

4.2 Depolarization-channel characterization

The determination of the backscatter coefficients, extinction coefficients and depolarization ratios depends on the transmission of the detection channels that can be different for light with different polarization directions. Baars (2012) cited and derived these relations in a detailed manner. Based on this findings, a short summary is given concerning the depolarization ratio using the transmission ration D of the depolarization channel. The ratio of the channel transmission efficiencies regarding parallel-polarized $\eta^{\|}$ and perpendicular-polarized $\eta^{\perp}$ light with respect to the polarization orientation of emitted laser light

$$\mathrm{D} = \frac{\eta^{\perp}}{\eta^{\|}} \tag{4.1}$$

is defined as transmission ratio (Mattis, 2002; Mattis et al., 2009). The transmission ratios of the four detection channels were investigated with a special setup for

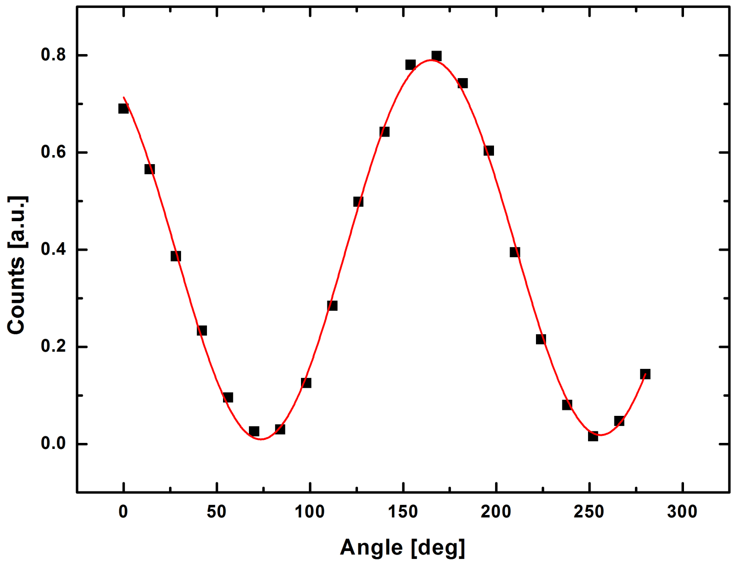

Figure 4.4: Transmission efficiency of the depolarization channel as a function of the angle of the polarization filter (black squares). The red line shows the fit using Eq. 4.2.

polarization dependent measurements. This setup consists of a combined deuterium and halogen light source (getLight-DHS by Sentronic GmbH, Germany), an optical fiber, a collimating lens, and a motorized rotary positioning polarization filter for polarizing the light output from this setup. The linear-polarized light is reflected from the mirrors of the telescope into the receiver unit with its detection channels. Rotating the polarization filter changes the polarization orientation of the incident light. The PMT detector of each channel works in photon counting mode, thus the incident light is measured in counts. The result of this depolarization-channel characterizing measurement is shown in Fig. 4.4 (black squares). The combined sinusoidal linear fit

$$y = y_0 + Ax + B\sin\left(\frac{x - x_\mathrm{c}}{w}\right) \tag{4.2}$$

y_0 [counts]	A [counts/deg]	B [counts]	x_c [deg]	w [deg]
0.394	$4.853 \cdot 10^{-5}$	0.388	-63.169	29.036

was applied to determine the transmission ratio. By using this equation, the offset

y_0, the amplitude B, the angle offset x_c, the period w, and an possible linearly increasing light intensity change by the light source during the measurement. The linear term with the factor A has been included due to consider the time required to stabilize the intensity of light. Its low value of $A = 4.853 \cdot 10^{-5}$ counts/$\circ$ shows that the light intensity was already almost stabilized before the measurement. Hence, the transmission ratio can be determined with

$$\mathrm{D} = \frac{y_0 + B}{y_0 - B} \tag{4.3}$$

giving a value for the depolarization channel of $\mathrm{D}_\mathrm{depol} = 130.33$ that had been used for the calculation of the particle depolarization ratio.

The determined transmission ratios of the other three channels (shown in appendix 7.3) revealed no significant sinusoidal behaviour and no significant correlation of the orientation of the polarization filter with the channel-transmission efficiencies. Hence, the proposed Eq. 4.3 was not applied to these channels.

4.3 Influence of the relaxation time of excited states of iodine vapour on HSRL signals

As discussed by Oelsner (Oelsner, 2012), the transmission of the iodine-vapour cell in BERTHA is non negligible at the maximum of the absorption line. A fraction of the light backscattered by particles can actually pass the iodine-vapour cell. This behaviour is called "cross talk", the respective parameter was determined by Oelsner to $\kappa_\mathrm{p} = (6.3 - 7.4) \cdot 10^{-3}$ for the iodine cell used in BERTHA. Although this assumption of a static cross talk parameter works fine for the most cases of high clouds, for cloud layers at low altitudes it has significant effects. In Fig. 4.5 profiles of particle backscatter and particle extinction coefficients are shown that had been determined with the Raman and with the HSR method. This measurement case was taken with BERTHA at the Leibniz Institute for Tropospheric Research Leipzig on 31-07-2012. It can be seen in Fig. 4.5 that the HSR method underestimates

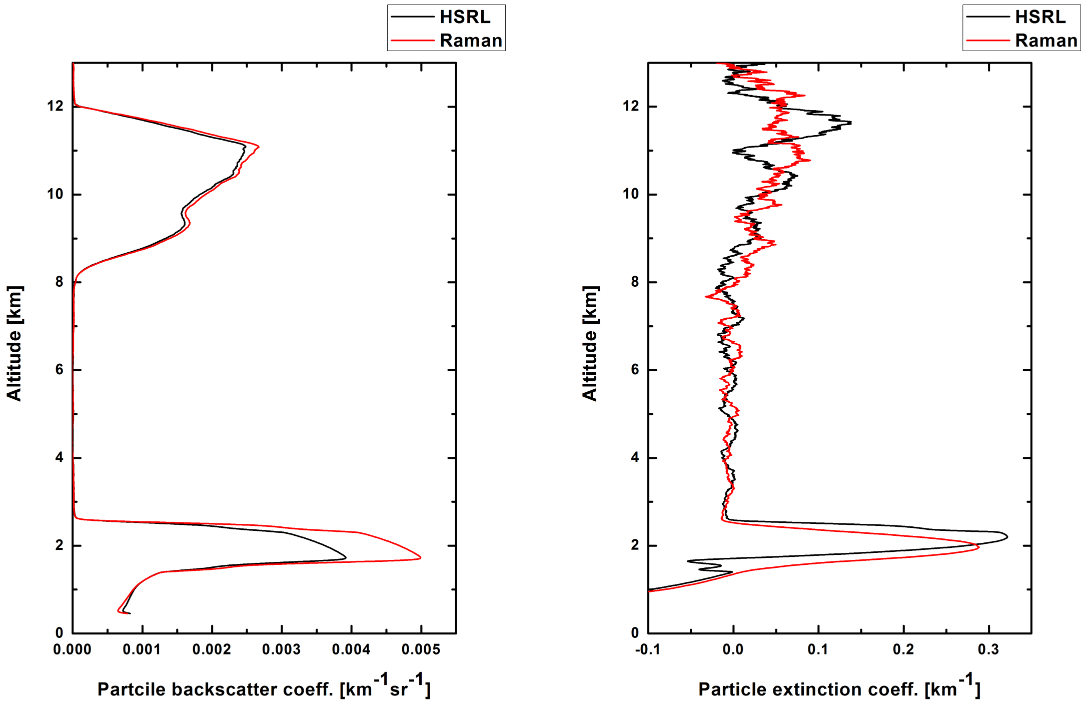

Figure 4.5: Profiles of particle backscatter and particle extinction coefficient determined with Raman and HSR method assuming no relaxation time of the excited vibronic states of iodine vapour and a constant suppression of the backscattered light from particles by the HSR channel of $\kappa_p = 6.3 \cdot 10^{-3}$ (31-07-2012).

the particle backscatter coefficient within the range from 1000 m to 2500 m altitude compared to that determined with the Raman method. Also, the HSR method underestimates the particle extinction coefficient an altitude of 1800 m and then overestimates it at 2200 m altitude. In this altitude range, the extinction coefficient maximum retrieved with the HSR method is at a higher altitude compared to that retrieved with the Raman method. In contrast, the profiles of the particle backscatter coefficient retrieved with the HSR and the Raman method, respectively, are very similar in the range of 8000 m to 12000 m altitude. The profiles of the particle extinction coefficient retrieved with the HSR and the Raman method, respectively, shows the same behaviour in this altitude range and match with their mean values. Considering a fraction of particle backscattered light passing the iodine-vapour cell, Oelsner (2012) used a modified equation for the HSRL signal:

$$\begin{aligned} P_{\mathrm{HSRL}}(R,\lambda_{\mathrm{HSRL}}) = K(\lambda_{\mathrm{HSRL}})\, G(R)\, [\kappa_{\mathrm{m}}\, \beta_{\mathrm{mol}}(R,\lambda_{\mathrm{HSRL}}) + \kappa_{\mathrm{p}}\, \beta_{\mathrm{par}}(R,\lambda_{\mathrm{HSRL}})] \\ \times T(R,\lambda_0)\, T(R,\lambda_{\mathrm{HSRL}})\ . \end{aligned} \tag{4.4}$$

Hence, the assumption of a constant cross talk parameter shows good agreement of the results retrieved with these two methods for those clouds at higher altitudes.

A fraction of backscattered light from the atmospheric molecules is attenuated by the iodine-vapour filter. This fraction is a function of altitude since the intensity of Rayleigh-Brillouin backscattered light depends on atmospheric temperature and pressure. According to Oelsner (2012), this molecular transmission factor results from the convolution of the iodine-vapour filter characteristic $\tau_{\mathrm{J}_2}(\nu)$, the Rayleigh-Brillouin spectrum $Y(\nu, T_{\mathrm{emp}}, p)$ and the laser spectrum $l(\nu)$ normalized to the convolution of $Y(\nu, T_{\mathrm{emp}}, p)$ and $l(\nu)$:

$$\kappa_{\mathrm{m}}(T,p) = \frac{\int\int \tau_{\mathrm{J}_2}(\nu) Y(\nu', T_{\mathrm{emp}}, p) l(\nu-\nu') d\nu' d\nu}{\int\int Y(\nu', T_{\mathrm{emp}}, p) l(\nu-\nu') d\nu' d\nu}\ . \tag{4.5}$$

A fraction of particle backscattered light is not completely attenuated by the iodine-vapour cell. Oelsner (2012) took this fact into consideration by including a constant transmission factor for particle backscatterd light κ_{p} and tried to determine it empirically with good results for high clouds (Fig. 4.5).

Due to the coaxial design and the high laser pulse energy of $600\,\mathrm{mJ}$ at $532\,\mathrm{nm}$ a non negligible fraction of emitted light is scattered into the telescope (Fig. 4.1, 16) before the laser pulse is transmitted into the atmosphere. According to Schuldt (2003), this causes a saturation effect leading to a population inversion of the I_2 spectral transition line $\#1109$ and thus to an increase of κ_{p}. The relaxation process of excited I_2 molecules can be radiative and non radiative.

Taking into account this saturation effect, detailed examination of κ_{p} revealed an exponential decay with increasing altitude as shown in Fig. 4.7. Different values of κ_{p} were found to adapt the HSRL signal to the Raman signal for the measurement cases 31-07-2012, 12-08-2012, and 15-08-2012 at different values of altitude (shown in Fig. 4.7). The red line in Fig. 4.7 shows the corresponding

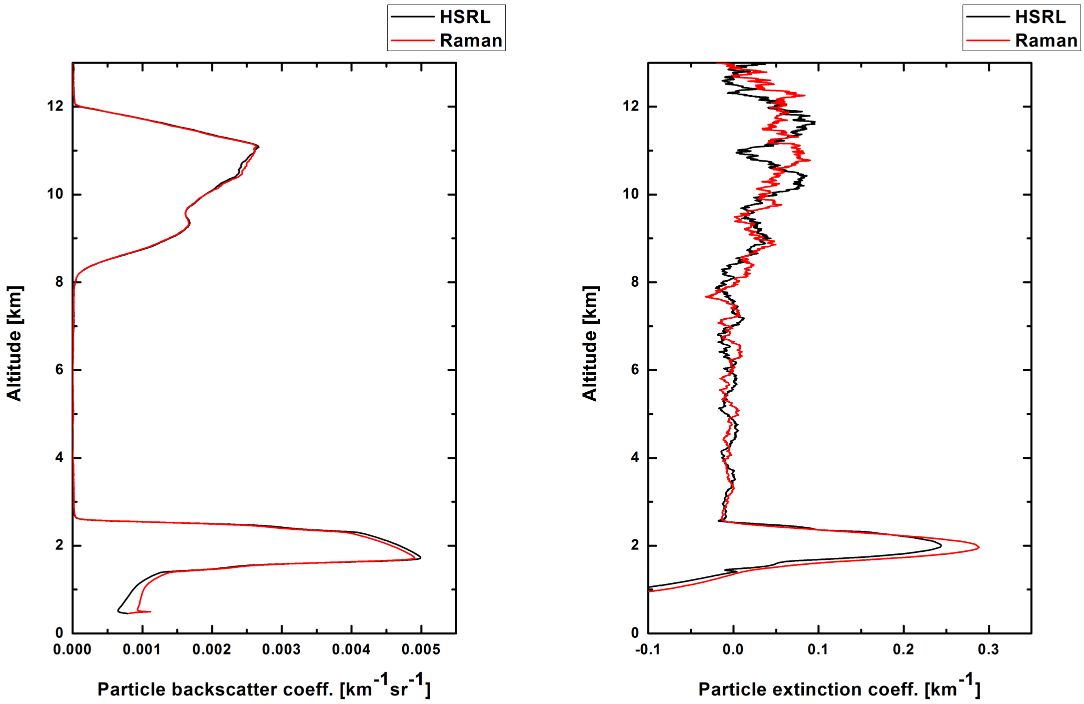

Figure 4.6: Profiles of particle backscatter and particle extinction coefficient determined with Raman and HSR method assuming the mean decay time of excited vibronic states of iodine vapour to $\tau_{\text{dec}} = 5\,\mu\text{s}$ and the constants $\kappa_p^0 = 9 \cdot 10^{-3}$, $\kappa_p^1 = 9 \cdot 10^{-2}$ (31-07-2012).

exponential decay function with a mean decay time of $\tau_{\text{dec}} = 5\,\mu\text{s}$, corresponding to a distance of $1500\,\text{m}$.

Relaxation process	Decay constant	Description
$I_2^* \longrightarrow I_2 + h\nu$	k_r	fluorescence
$I_2^* \longrightarrow I + I$	k_{nr}	dissociation
$I_2^* + I_2 \longrightarrow I + I + I_2$	k_s	collisional dissociation

According to Masiello et al. (2003), the overall decay constant for exited states of iodine vapour is the sum of the individual decay constants

$$k = \frac{1}{\tau_{\text{dec}}} = k_r + k_{nr} + k_s \frac{p(I_2)}{k_B T_{\text{emp}}} \tag{4.6}$$

and depends on the pressure of iodine vapour $p(I_2)$ and its thermodynamically energy $k_B T_{\text{emp}}$. In Fig. 4.8 the increase of lifetime for decreasing values of pressure

$p(\mathrm{I}_2)$ is shown. Hence, the number concentration of excited states becomes

$$\mathrm{n}(t) = \mathrm{n}_0 \exp\left\{-t\left[\mathrm{k}_r + \mathrm{k}_{nr} + \mathrm{k}_s \frac{p(\mathrm{I}_2)}{\mathrm{k}_\mathrm{B} T_\mathrm{emp}}\right]\right\} \ , \tag{4.7}$$

in which n_0 is the initial concentration of excited iodine (i.e., immediately after the laser pulse) and t is the time after excitation. The transmission of the iodine cell for backscattered light from particles is related to the number concentration of excited states for the spectral transition line $\#1109$ by

$$\begin{aligned} \kappa_\mathrm{p}(t) &= \kappa_\mathrm{p}^0 + \sigma_\mathrm{a}\,\mathrm{n}(t)\,l \\ \kappa_\mathrm{p}(z) &= \kappa_\mathrm{p}^0 + \kappa_\mathrm{p}^1 \exp\left\{-\frac{2z}{c\,\tau_\mathrm{dec}}\right\} \end{aligned} \tag{4.8}$$

a constant transmission factor κ_p^0 referring to the case of enough iodine molecules not being excited and, an initiated transmission factor κ_p^1 referring to the number of excited iodine molecules by the the emitted laser pulse, the specific absorption cross section σ_a, the length of the iodine cell l, the time after the initiated excitation $t = 2z/c$, the altitude z and the speed of light c.

The particle backscatter and extinction profiles are changed by using $\kappa_\mathrm{p}(t)$ instead of the constant κ_p^0. This is exemplarily shown for the measurement case of 31-07-2012 in Fig. 4.6. Here, the particle backscatter and extinction coefficients have been determined using the time dependent $\kappa_\mathrm{p}(t)$ function of Eq. 4.8. As can be seen in Fig. 4.6, the previously discussed differences (especially the vertical shifts) mainly disappear.

There is still an underestimation of the extinction coefficient around $2000\,\mathrm{m}$ altitude by the HSR method. This underestimation could not be investigated within this study, might be caused by overlap effects and will be subject to further investigations.

The parameters of Eq. 4.8 have been found by fitting the profiles determined with the HSR method to the profiles determined with the Raman method for three measurement cases (31-07-2012, 12-08-2012 and 15-08-2012) and in the altitude region from $500\,\mathrm{m} - 9600\,\mathrm{m}$. The fit shown in Fig. 4.7 yields the constant transmission factor, the initiated transmission factor and the relaxation time of the excited iodine states. The results are $\kappa_\text{p}^0 = 9 \cdot 10^{-3}$, $\kappa_\text{p}^1 = 9 \cdot 10^{-2}$ and $\tau_\text{dec} = 5\,\mu\text{s}$. The constant transmission factor is very close to the transmission factor determined by Oelsner (2012). This factor can be considered as transmission factor in case of no saturation effects. The initiated transmission factor defines the additionally reduction of absorption capability by the iodine-vapour cell initiated due to the saturation effect. The determined mean decay time $\tau_\text{dec} = 5\,\mu\text{s}$ is about double of the relaxation time of neighbouring fluorescence levels determined by Masiello et al. (2003) for the pressure of $28.7\,\text{Pa}$. The pressure of $28.7\,\text{Pa}$ is less than $62.3\,\text{Pa}$, which is the vapour pressure of iodine at $30\,^\circ\text{C}$. Since it is not possible to measure the actual vapour pressure inside the used iodine cell, these discrepancies could not be investigated within this study.

As a consequence of the discussed saturation effect, an additionally transition line broadening should be expected as discussed by Schuldt (2003). Spectral transitions are not infinite fine. In addition to the natural line broadening as the lower limit, other line broadening effects have to be taken into account (Demtröder, 2000). If the transition probability is equal for all molecules, the corresponding line broadening is called homogeneous and the transition depends not on an additional parameter. Oelsner (2012) discussed the natural line broadening (homogeneous), Doppler broadening (inhomogeneous) and pressure broadening (homogeneous). Based on the absorption coefficient for a naturally line broadened transition (Demtröder, 2000)

$$\alpha_\text{abs}(\omega) = \frac{\left(\frac{\gamma}{2}\right)^2}{(\omega - \omega_0)^2 + \left(\frac{\gamma}{2}\right)^2} \tag{4.9}$$

with the FWHM γ and the central angular frequency ω_0 of the transition line, the absorption coefficient can be described for saturation broadening.

For homogeneous broadened lines the additional broadening by saturation (Demtröder, 2000) yields to a modified value of the FWHM of the absorption coefficient dependency on the frequency

$$\gamma_\text{sat} = \gamma\sqrt{1 + S_0} \tag{4.10}$$

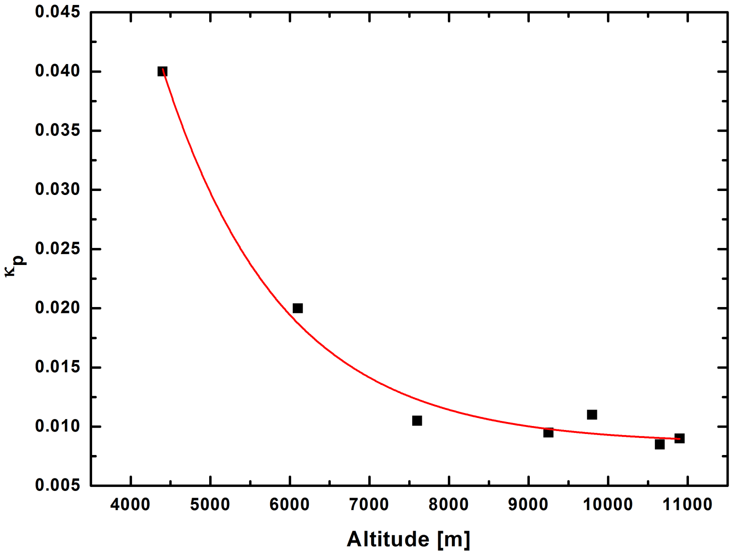

Figure 4.7: Plot of transmission factor for particle backscattered light κ_p versus altitude (black squares), and a corresponding exponential decay function with a mean decay time of $\tau_\mathrm{dec} = 5\,\mu\mathrm{s}$ corresponding to a distance of $1500\,\mathrm{m}$ (red line).

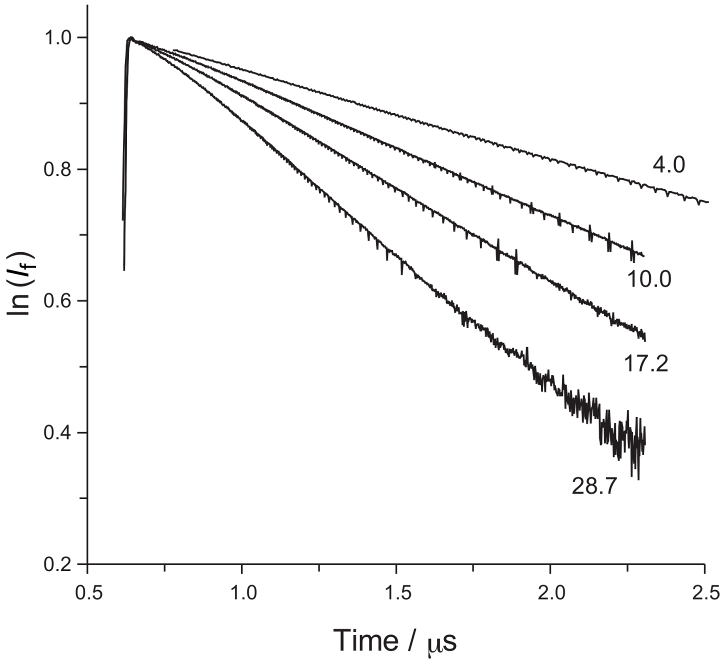

Figure 4.8: Plot of logarithmic fluorescence intensity $ln(I_f)$ versus time for I_2 for different pressure values [Pa]. The decay constant $-$k can be read from the slope of each plot (Fig. adopted from Masiello et al. (2003)).

that depends additionally on the saturation parameter

$$S_0 = \frac{I}{I_{\text{sat}}} \,. \tag{4.11}$$

This parameter is the fraction of incident light intensity I to the saturation light intensity I_{sat}, an intensive property of each transition line. I_{sat} can be determined by spectral absorption spectroscopy and has the value $I_{\text{sat}} = 0.985\,\text{mW/mm}^2$ for the neighboured transition line 1105 (Schuldt, 2003). Hence, the value of I_{sat} for the transition line $\#1109$ can be estimated to be in the same order of magnitude.

According to Demtröder (2000) and with Eq. 4.10, and Eq. 4.11 taken into account, Eq. 4.9 yields to

$$\alpha_{\text{sat}}(\omega) = \alpha_{\text{abs}}(\omega_0) \frac{\left(\frac{\gamma}{2}\right)^2}{(\omega - \omega_0)^2 + \left(\frac{\gamma_{\text{sat}}}{2}\right)^2} \,. \tag{4.12}$$

As a conclusion, the discovered decay of the transmission factor for particle scattered light κ_p was discussed in terms of the relaxation time of excited states of iodine vapour and an exponential function was proposed to describe it. This function is motivated by the saturation effect which is known from fluorescence spectroscopy and results in a good matching between the HSRL and Raman retrieved profiles of particle backscatter and particle extinction coefficient. The saturation effect depends mainly on the incident light intensity (Eq. 4.11). The described double cone shaped way of light in the iodine-vapour cell (described in subchapter 4.1) might enhance the saturation effect. As a consequence, an additional broadening effect due to saturation has to be considered. Further investigations are necessary to examine and compare the shown results. It appears possible to retrieve the particle lidar ratio solely with the HSR channel, if the parameters of saturation dependent filter transmittance and its influence on the received HSR signal are well known.

4.4 Measurement of cirrus clouds on 31-07-2012

The following measurement was taken at the Leibniz Institute for Tropospheric Research in Leipzig on 31-07-2012. The temporal development of the range corrected signal at $532\,\mathrm{nm}$ wavelength is shown in Fig. 4.9 for the time period between 20:14 UTC and 22:44 UTC. Occasionally a layer at $2\,\mathrm{km}$ altitude reduced the signal from higher altitudes significantly, so the time period between 21:38 UTC and 22:44 UTC was used for data retrieval. The used radiosonde data were taken from the WRF-model to get the temperature and pressure profiles. During this measurement a cirrus cloud was present with a cloud base altitude of $8\,\mathrm{km}$ and a geometrical depth of $3-4\,\mathrm{km}$.

As can be seen in Fig. 4.9, the altitude and optical depth of this layer decreased with time. The corresponding temporal development of the range corrected particle depolarization signal at $532\,\mathrm{nm}$ wavelength is shown in Fig. 4.10. This signal remained nearly constant at the altitude between $8\,\mathrm{km}$ and $12\,\mathrm{km}$.

As discussed in subchapter 4.3, a crosstalk of backscattered light from particles influences the measurement by the HSR channel. This can be seen when the temporal development of the range corrected HSR signal (Fig. 4.12) is compared with the total signal (Fig. 4.9). The light scattered by particles at an altitude of $2\,\mathrm{km}$ detected in the total channel is also detected in the HSR channel. However, the light backscattered by particles should be suppressed by the iodine-vapour cell and thus the HSR channel is supposed be comparable to the Raman channel (Fig. 4.11) in the retrieved signals. Considering this crosstalk with a distance dependent exponential decay law for the transmission factor $\kappa_\mathrm{p}(z)$ (Eq. 4.8) yields to the profiles of the particle extinction and backscatter coefficients (Fig. 4.6).

The retrieved profiles of particle depolarization ratio and particle lidar ratio are smoothed over 121 bins. This means the measured values of the cirrus cloud are only independent of atmospheric volumes outside the cirrus cloud if the chosen measurement altitude is at a minimum distance of $453.75\,\mathrm{m}$ inside the cirrus cloud. Hence, the average values of particle depolarization ratio and particle lidar ratio

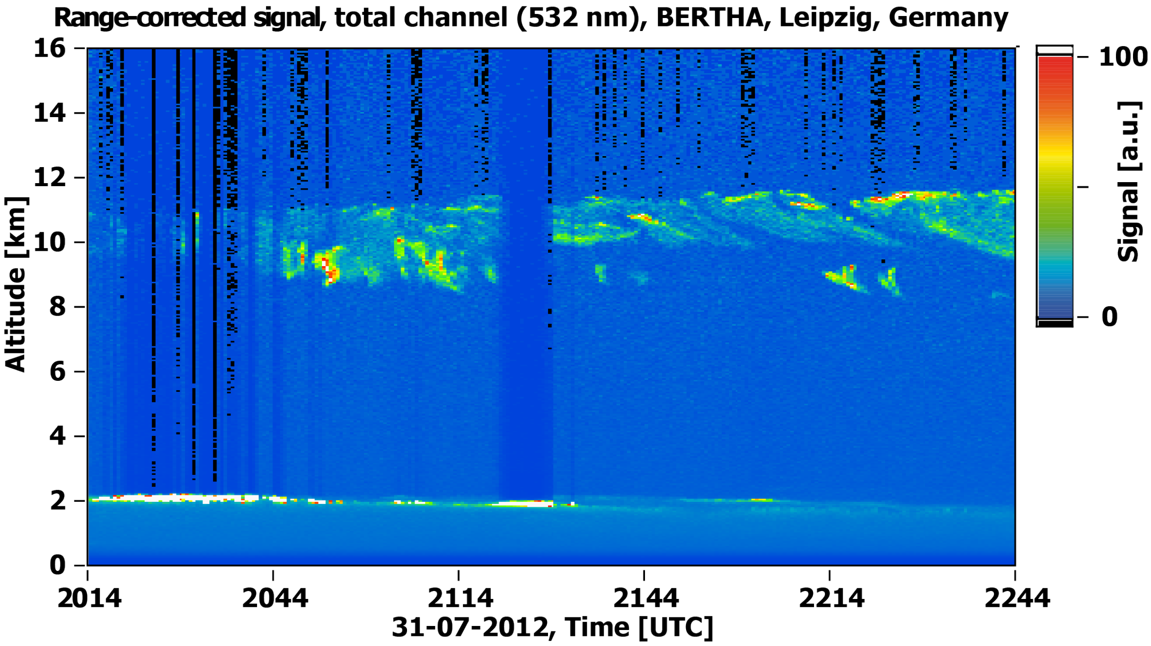

Figure 4.9: Range corrected signal at 532 nm wavelength, total channel.

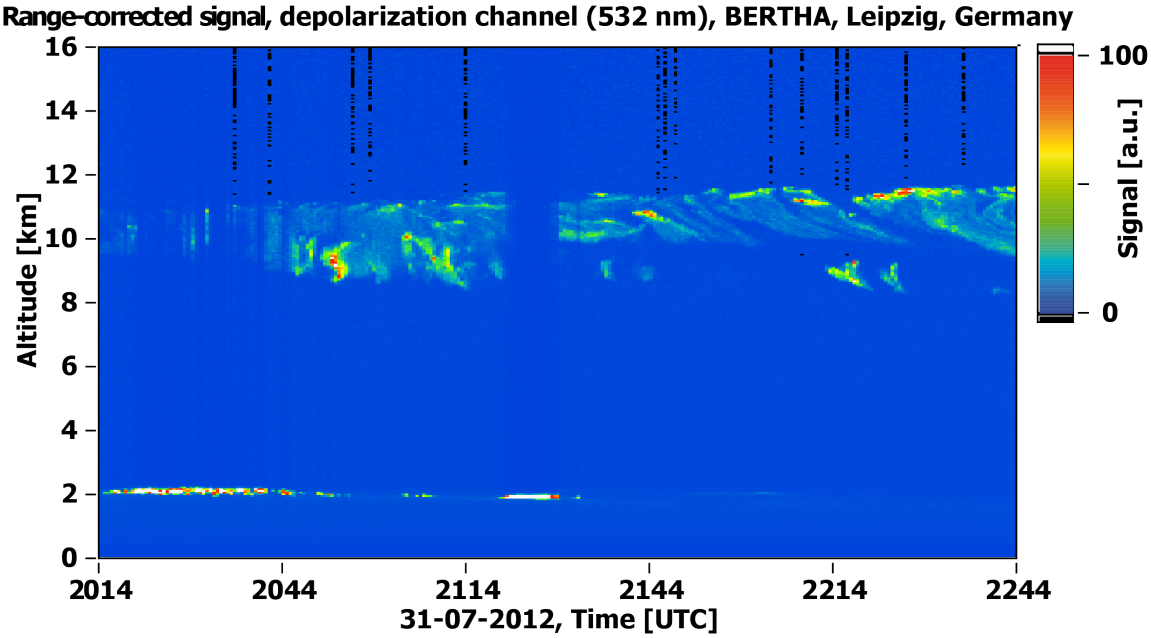

Figure 4.10: Range corrected signal at 532 nm wavelength, depolarization channel.

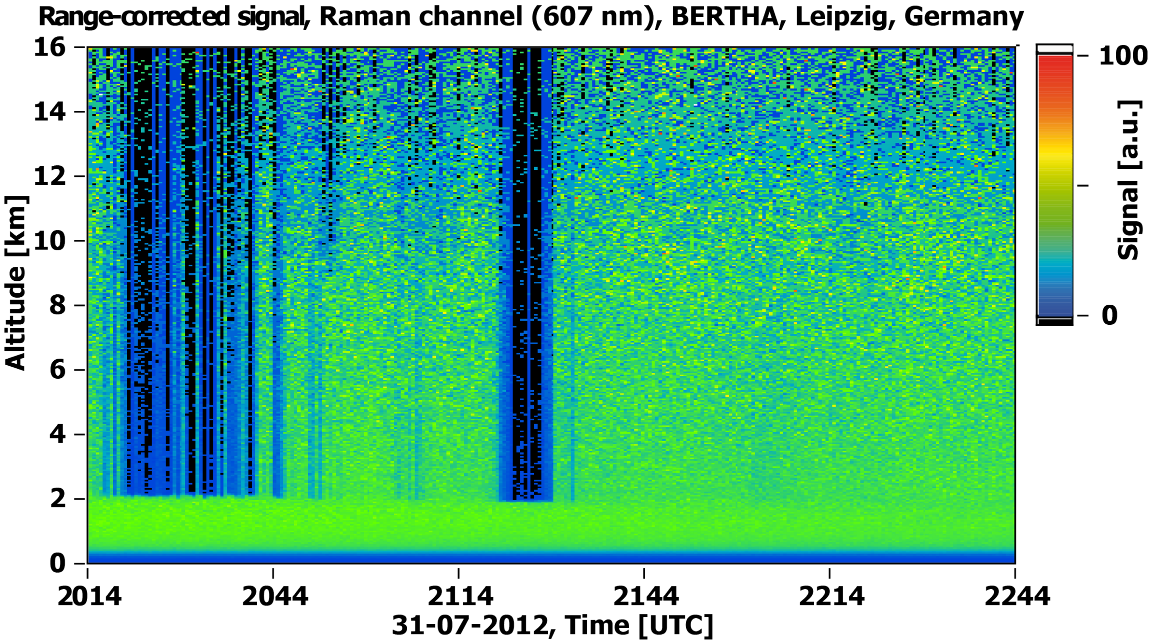

Figure 4.11: Range corrected signal at 607 nm wavelength, Raman channel.

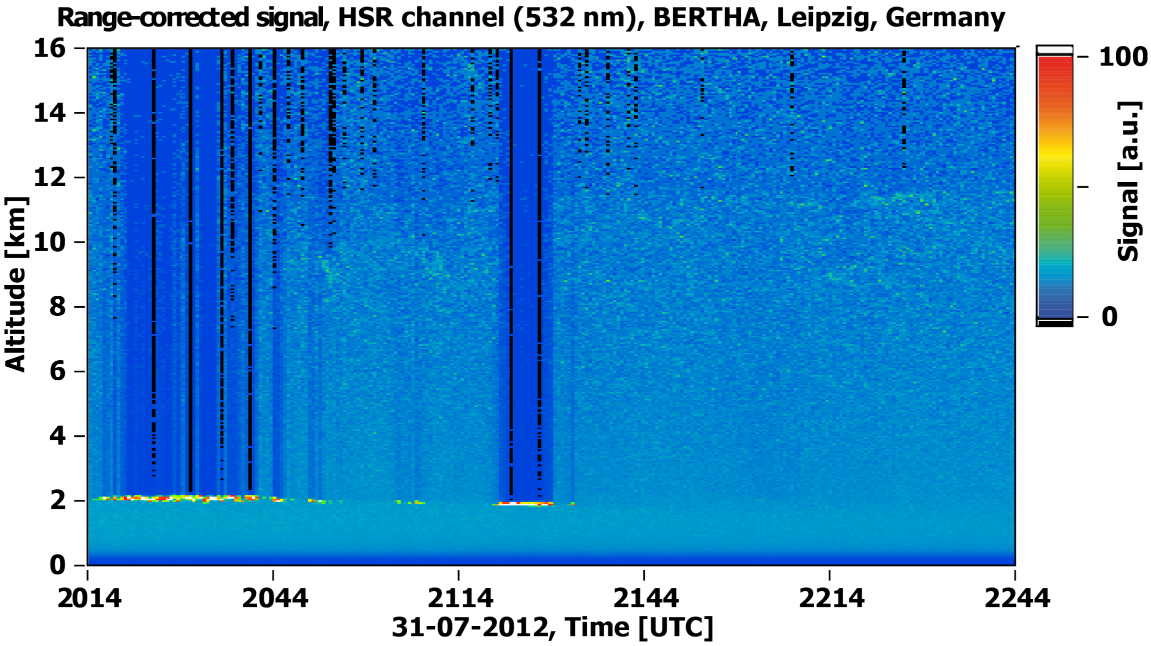

Figure 4.12: Range corrected signal at 532 nm wavelength, HSR channel.

were determined in the altitude range from $10\,\mathrm{km}$ to $11\,\mathrm{km}$. In this altitude range, the molecular and particle depolarization ratio remains approximately constant. It varied between $\delta_{\mathrm{par}} = 6.9\%$ and $\delta_{\mathrm{par}} = 8.4\%$ and has an average value of $\delta_{\mathrm{par}} = 7.2\%$. The corresponding average value of the particle lidar ratio has been determined to $\mathrm{S}_{\mathrm{par,Ra}} = 25\,\mathrm{sr}$ using the Raman method and to $\mathrm{S}_{\mathrm{par,HSRL}} = 20\,\mathrm{sr}$ using the HSR method. The particle lidar ratio varied between $\mathrm{S}_{\mathrm{par,Ra}} = 13\,\mathrm{sr}$ and $\mathrm{S}_{\mathrm{par,Ra}} = 38\,\mathrm{sr}$ if it has been determined with the Raman method and between $\mathrm{S}_{\mathrm{par,HSRL}} = 2\,\mathrm{sr}$ and $\mathrm{S}_{\mathrm{par,HSRL}} = 33\,\mathrm{sr}$ if it has been retrieved with the HSR method.

To conclude, the retrieved particle lidar ratios are in the range of the formerly measured and calculated values (appendix 7.2). But the determined particle depolarization ratios are smaller than the formerly measured and calculated values (appendix 7.2). There are two main reasons for these unusually low values of particle depolarization ratio. One possible explanation is the presence of small crystals in the size region of a few microns as described by Liou et al. (2000). But according to Yang and Liou (2000), the corresponding particle lidar ratios should then be larger than $120\,\mathrm{sr}$. The second explanation is instrumental. According to Freudenthaler et al. (2009), the reason for the observed unusual low particle depolarization ratios could be due to several instrumental uncertainties. A small misalignment of the polarization filter in the receiver with respect to the polarization orientation output laser-beam can lead to large errors. To solve the problem, a so called $\pm 45°$-calibration method is presented in Freudenthaler et al. (2009). This method is more robust against misaligned calibration angles as shown in Freudenthaler et al. (2009). To implement this calibration method to the lidar system BERTHA, a motorized polarization filter is proposed to be installed as described in the following subsection.

4.5 Contributions to complete the receiver of the lidar system BERTHA, an outlook

At the moment the particle depolarization ratio and particle lidar ratio can be determined at daytime with the HSR method, and at nighttime with the HSR method and Raman method. This setup showed capabilities for investigations of atmospheric ice particles. However, further modifications are necessary to reduce, or better to eliminate, the occurring crosstalk in the HSR channel and to calibrate the depolarization channel with the $\pm 45°$-calibration method. Additionally, more channels will be installed to investigate the particle depolarization ratio at three wavelengths, the backscatter coefficient at three wavelengths, the extinction coefficient at three wavelengths, the water vapour mixing ratio and the tropospheric temperature profile. Also, a motorized aperture will be installed to prepare the lidar system for measurements at several FOVs.

The current and the future receiver setup can be compared using Figs. 4.13 and 4.14. An off-axis parabolic mirror (Fig. 4.13, 1) collimates the incident light and reflects it into the setup of beam splitters. Simulations with the ray tracing software Zemax (Zemax Development Corporation, 2010) revealed a critically image slant of the primary parabolic mirror surface caused by the off-axis parabolic mirror. Hence, the off-axis parabolic mirror will be replaced by two collimating lenses and a deflecting flat mirror (Fig. 4.15, 5 and 6). These three optical elements will be mounted together on top of a compact-unit (Fig. 4.15), which also contains a stray light protector to improve the signal-to-noise ratio, a motorized aperture and a motorized rotary-positioning polarization-filter. This adjustable polarizing filter will be installed to fulfil the requirements of implementing an automated $\pm 45°$-calibration method. The motorized aperture opens the possibility of multiple-FOV measurements that would allow investigations to the particle sizes in cirrus clouds (Eloranta and Kuehn, 2002). The lidar system is designed to detect inelastically backscattered light, elastically backscattered light and linear-depolarized backscattered light. Therefore

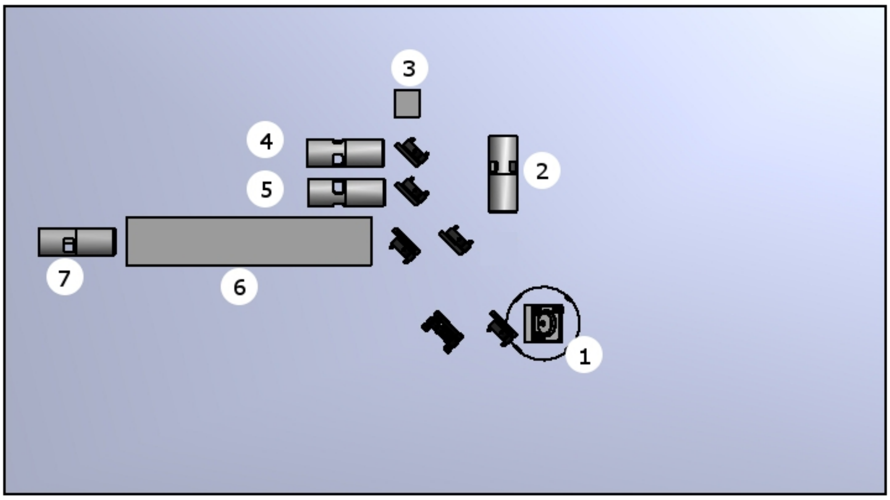

Figure 4.13: The receiver of BERTHA. 1: Off-axis parabolic mirror, 2: Raman channel (607 nm), 3: Camera, 4: Total channel (532 nm), 5: Depolarization channel (532 nm), 6: Iodine-vapour cell, 7: Detector for the HSR channel, Mirrors and beam splitters are drawn black. Designed with Inventor 2013 (Autodesk Inc., 2012).

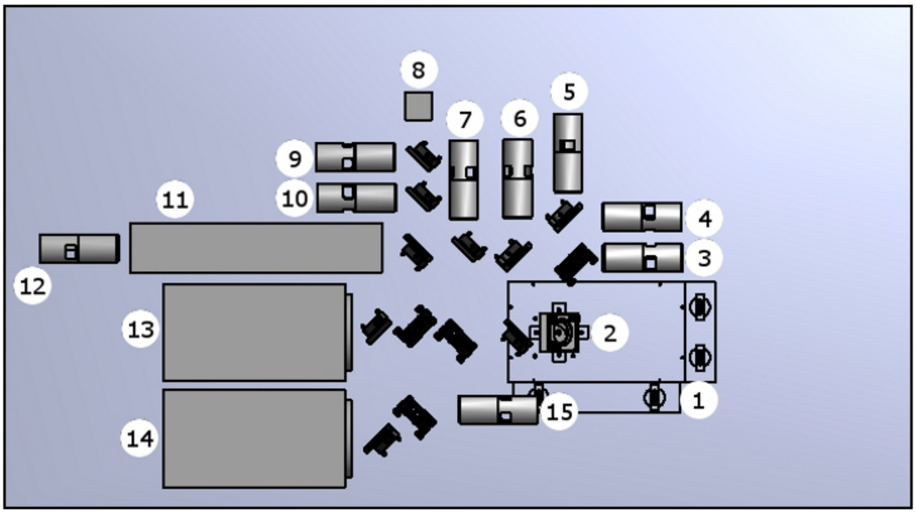

Figure 4.14: The receiver of the complete lidar system BERTHA. 1: Compact-unit housing, 2: Deflecting flat mirror, 3: Raman channel (387 nm), 4: Depolarization channel (355 nm), 5: Total channel (355 nm), 6: Raman channel (407 nm), 7: Fiber optic coupling unit to rotational Raman channels for temperature measurements, 8: Camera, 9: Total channel (532 nm), 10: Depolarization channel (532 nm), 11 and 12: HSR channel, 13: Total channel (1064 nm), 14: Depolarization channel (1064 nm), 15: Raman channel (607 nm), Mirrors and beam splitter are drawn black. Designed with Inventor 2013 (Autodesk Inc., 2012).

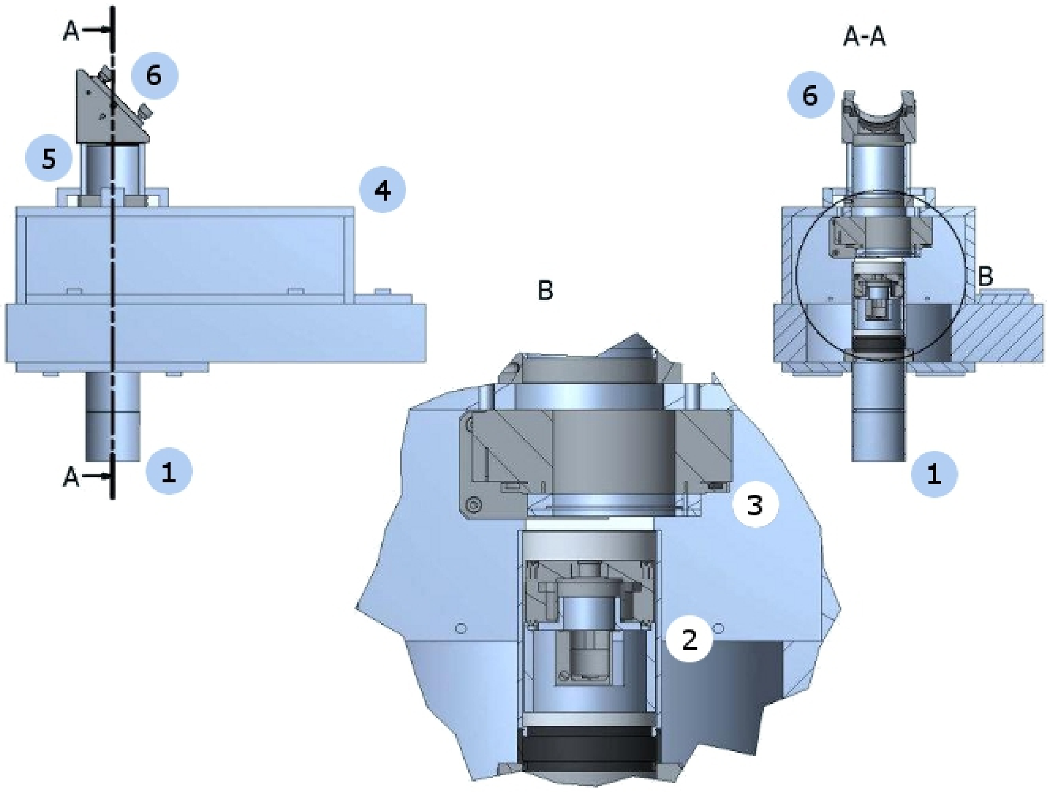

Figure 4.15: Compact-unit consisting of 1: Stray light protector, 2: Motorized aperture, 3: Motorized rotatable polarization filter, 4: Housing, 5: Lens tube with collimator, 6: Deflecting flat mirror. Designed with Inventor 2013 (Autodesk Inc., 2012).

the system will have five channels for detection inelastically backscattered light at 387 nm, 407 nm, 532 nm, and 607 nm wavelength. The elastically backscattered light will be detected by three channels, at 355 nm, 532 nm and 1064 nm wavelength. The Doppler broadened backscattered light will be detected by 532 nm wavelength using the HSR method. The linear depolarization will be detected by three channels at 355 nm, 532 nm and 1064 nm. To suppress the discussed crosstalk, the optical design of the HSR channel will be changed. Currently, the illuminated volume inside the iodine cell has a double cone shape (Fig. 4.1, 13) to ensure no shading and reflection effects. But as discussed in subchapter 4.3, it is supposed that this shape of illuminated volume enhances the crosstalk since the energy density gets larger at the apexes. In order to ensure a cylindrical shaped illuminated volume inside the iodine-vapour cell, the optical design will be changed.

5 Particle lidar ratios and particle depolarization ratios of cirrus clouds

Measurements with BERTHA not only require complex and time-consuming preparations but also a constant monitoring. For this reason, the intensive properties particle lidar ratio and particle depolarization ratio of cirrus clouds are retrieved out of long-term measurements with the automated depolarization Raman lidar Polly^{XT}. In the following this lidar system is briefly described and an example measurement is presented. The data measured at the Leibniz Institute for Tropospheric Research Leipzig are presented and discussed in the last subchapter.

5.1 Lidar system Polly^{XT}

The compact and automated multi-wavelength polarization Raman lidar Polly^{XT} (POrtable Lidar sYstem eXTended) is a so called $3+2+1$ system. It emits light at three wavelengths and allows the determination of the particle backscatter coefficient at three wavelengths, the particle extinction coefficient at two wavelengths and the particle depolarization ratio at one wavelength. The system is described by Althausen et al. (2009) in detail and Engelmann et al. (2012). The following system information are from these publications and presented without explicit citing.

Polly^{XT} is housed in a rainproof cabinet. Its major parts are shown in Fig. 5.1. Basically, Polly^{XT} consists of three main components. These are the emitter, the receiver with data acquisition and the equipment for housing the optics and electronics. On the emitter side, a Nd:YAG laser (Continuum Inlite III) emits laser light pulses at 1064 nm wavelength with a repetition rate of 20 Hz. These pulses are frequency doubled to 532 nm wavelength and tripled to 355 nm wavelength with second and third harmonic generating crystals (Fig. 5.2, E0, SHG & THG). The corresponding pulse energies are 180 mJ/pulse at 1064 nm wavelength, 110 mJ at 532 nm wavelength, and 60 mJ/pulse at 355 nm. The laser light diameter of 6 mm is increased to 45 mm by a beam expander (Fig. 5.2, E3). Thus, the beam divergence of the laser light emitted into the troposphere is reduced from 1.5 mrad to below 0.2 mrad.

On the receiver side, a Newtonian telescope with a main mirror diameter of 30 cm, a focal length of 0.9 m and a FOV of 1 mrad collects the backscattered light. The received light is reflected through a pinhole (Fig. 5.2, R3) into the receiver. Inside the receiver, the incident light is separated by dichroitic beam splitters and a polarizer and detected by seven photo-multiplier-tube (PMT) detectors working in photon counting mode. Fast Comtec data acquisition cards are used to acquire the received data (Fig. 5.1, 7). The spatial resolution of the data acquisition is 30 m. A computer is used to store the acquired data with a temporal resolution of 30 sec and to control the overall system performance.

In this study, the channel for measuring the elastic-backscattered signal at 532 nm wavelength, the channel for measuring the depolarized signal at 532 nm wavelength and the channel for measuring the Raman backscattered signal from atmospheric nitrogen molecules at 607 nm wavelength are used. The corresponding FWHM of the filter bandwidth are 1.12 nm, 1.12 nm and 0.31 nm. Contrary to BERTHA, no HSR channel is installed in Polly^{XT} and hence no measurement of the particle lidar ratio is possible during daytime. A motorized filter wheel with polarizing filters in different orientations is installed for the calibration of the depolarization channel.

Figure 5.1: The depolarization Raman lidar system Polly^{XT} in its rainproof cabinet. This figure is adopted from Althausen et al. (2009). 1: Laser head, 2: Laser power supply, 3: Beam expander, 4: Receiver telescope, 5: Receiver with seven channels, 6: Power supply, 7: Computer with data acquisition and interface cards, 8: UPS, 9: Air conditioner, 10: Sensor for outdoor temperature and rain, 11: Roof cover.

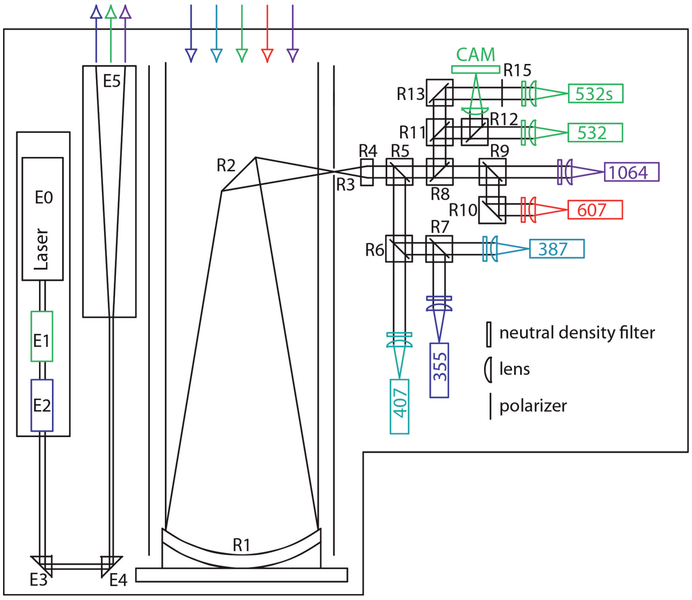

Figure 5.2: Optical setup of Polly^{XT}. E0: Laser, E1 & E2: Second and third harmonic generating crystals, E3 & E4: quartz prism, E5: Beam expander, R1: Primary mirror, R2: Secondary mirror, R3: Pinhole, R4: Achromatic lens, R5 - R13: Beamsplitter, R15: Polarization filter, CAM: Camera.

5.2 Calibration and measurement errors

The ratio between perpendicular polarized light and parallel polarized detected by a channel is its transmission ratio D. This ratio should be high for depolarization channels and for channels detecting unpolarized light it should be 1. According to Mattis et al. (2009), the uncertainty of retrieved lidar signals is higher than 5% when the transmission ratio of the total-backscatter channel is below 0.85 or higher than 1.15. As reported by Baars (2012), the total-backscatter signal at $532\,\mathrm{nm}$ wavelength depends on the polarization plane of incident light for Polly^{XT}. Thus, the measured depolarization signal has to be corrected. This is done in accordance to Grein (2006) and Mattis et al. (2009) as following:

$$P^{\mathrm{corr}}(R, 532\,\mathrm{nm}) = P^{\mathrm{meas}}(R, 532\,\mathrm{nm}) \frac{1 + \delta_{\mathrm{vol}}(R, 532\,\mathrm{nm})}{1 + \mathrm{D}_{532\,\mathrm{nm}}\, \delta_{\mathrm{vol}}(R, 532\,\mathrm{nm})} \,. \tag{5.1}$$

According to Baars (2012) the filter-dependent molecular depolarization has to be taken into account for the calculation of the particle depolarization ratio. The molecular depolarization signal consists of Cabannes line induced and rotational-Raman line induced depolarization. While the Cabannes line induces a molecular depolarization ratio of 0.00395 and contributes with 97.3% to the molecular backscattered light, the rotational-Raman line induces a molecular depolarization ratio of 0.75 and contributes with 2.7% to the molecular backscattered light (Baars, 2012). This distribution of the Raman lines depends on ambient-temperature and thus leads to a partially attenuation of the depolarization signal for narrow-band filters. This dependence on ambient-temperature affects the retrieval of the particle depolarization ratio and can be calculated in accordance to Wandinger (2005b) for known filter transmission curves.

The alignment uncertainty of the laser's polarization plane to the plane of the polarizer transmission leads to large errors of the received depolarization signal. According to Freudenthaler et al. (2009), due to the $\pm 45°$-calibration method these errors compensate each other for a large range of misalignments. Therefore, a motorized filter wheel containing polarizer perpendicular in their orientation of transmission is installed in Polly^{XT}.

For the lidar system BERTHA, Tesche (2011) used the Gaussian error propagation law to calculate the random error of the particle lidar ratio in terms of a random error in the particle backscatter and extinction coefficient as

$$\frac{\Delta S_{\text{par}}(R,\lambda_i)}{S_{\text{par}}(R,\lambda_i)} = \sqrt{\left(\frac{\Delta\alpha_{\text{par}}(R,\lambda_i)}{\alpha_{\text{par}}(R,\lambda_i)}\right)^2 + \left(\frac{\Delta\beta_{\text{par}}(R,\lambda_i)}{\beta_{\text{par}}(R,\lambda_i)}\right)^2}\ . \tag{5.2}$$

Tesche (2011) showed that this approach results in a value of 20% for the retrieved particle lidar ratio at $532\,\text{nm}$ wavelength. As the PMT-detector count-rates and the Raman-channel structure of BERTHA is comparable to those of Polly^{XT}, the uncertainty of the retrieved particle lidar ratio apply also to that of Polly^{XT}.

5.3 Measurement of cirrus clouds on 16-08-2012

Just like all measurements taken for this study, also this measurement has been taken at the Leibniz Institute for Tropospheric Research in Leipzig. The measurement on 16-08-2012 was selected to describe the procedure of data retrieval, combination and determination of deduced quantities in detail. Radiosonde data are used to calculate the molecular contribution. These data were taken from radio-soundings at the meteorologic observatory Lindenberg (WMO 10393 LINDENBERG) started at 00:00 UTC. This weather station is located approximately $150\,\text{km}$ in the north-east of Leipzig. The temporal development of the range corrected signal at $1064\,\text{nm}$ wavelength is shown Fig. 5.3 for the period between 19:20 UTC and 19:49 UTC. A cirrus cloud was present during this measurement period. The mean cloud base altitude was at $8.5\,\text{km}$, the geometrical depth of the cloud varied between $3\,\text{km}$ and $3.5\,\text{km}$. At the bottom of the cirrus cloud, the particle depolarization ratio at $532\,\text{nm}$ wavelength increases from 0% at $8\,\text{km}$ altitude to more than 40% at $8\,\text{km}$ altitude. This is an excellent example for the detection of cirrus clouds by retrieving the depolarization ratio out of lidar measurements as shown in Fig. 5.4. The particle depolarization ratio remains nearly constant at a mean value of 46% in the whole

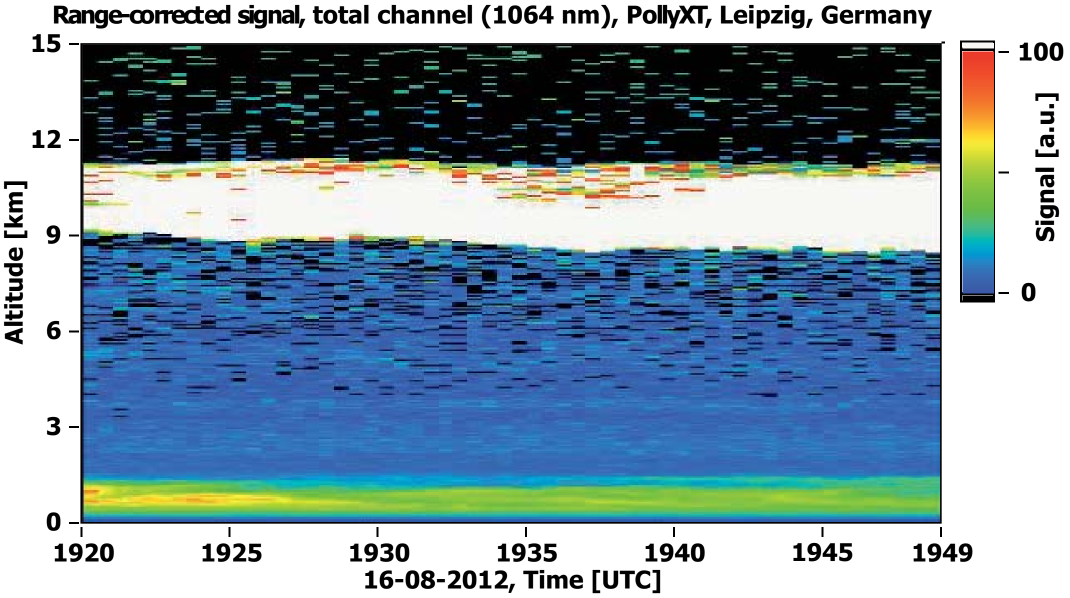

Figure 5.3: Range corrected signal at 1064 nm wavelength, total channel.

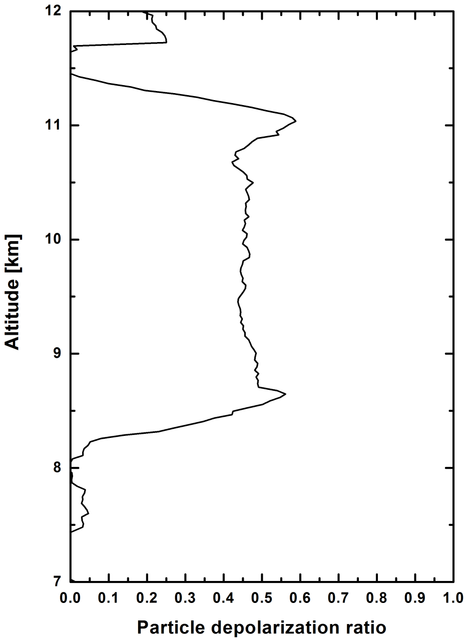

Figure 5.4: Particle depolarization-ratio profile at 532 nm wavelength (16-08-2012).

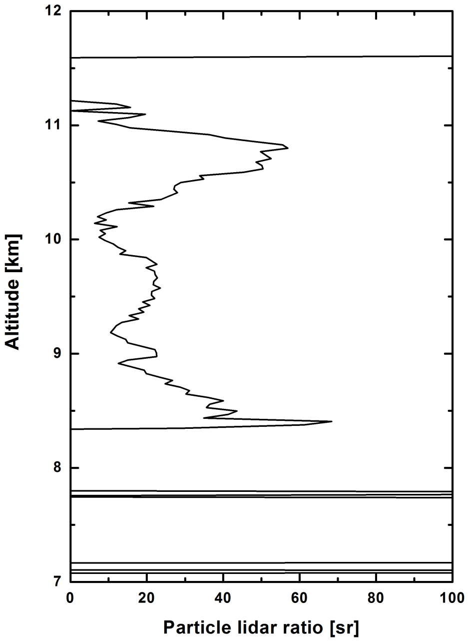

Figure 5.5: Raman retrieved particle lidar-ratio profile at 532 nm wavelength (16-08-2012).

altitude range between $9\,\mathrm{km}$ and $11\,\mathrm{km}$. At the top of the cirrus cloud, in the altitude range between $11\,\mathrm{km}$ and $12\,\mathrm{km}$ the particle depolarization ratio decreases to nearly 0% after a short increase. The particle lidar ratio at $532\,\mathrm{nm}$ wavelength decreases from more than $60\,\mathrm{sr}$ at an altitude of $8.4\,\mathrm{km}$ to a value of about $10\,\mathrm{sr}$ at an altitude of $9.2\,\mathrm{km}$. From this altitude until an altitude of $10.2\,\mathrm{km}$, the particle lidar ratio stays in the range between $5\,\mathrm{sr}$ and $25\,\mathrm{sr}$. In the altitude range from $10.2\,\mathrm{km}$ to $11.2\,\mathrm{km}$ the particle lidar ratio increases to more than $55\,\mathrm{sr}$ at $10.8\,\mathrm{km}$ and decreases to nearly $0\,\mathrm{sr}$ at $11.2\,\mathrm{km}$. The elaborated the particle depolarization ratio (Fig. 5.4) and the particle lidar ratio (Fig. 5.5) profiles are smoothed over 13 bins, which corresponds to $390\,\mathrm{m}$.

To summarize, the cirrus cloud is clearly identified by the retrieved values of particle depolarization ratios. The mean values of particle depolarization ratio and particle lidar ratio for this cirrus cloud were determined to 46% and $25\,\mathrm{sr}$ respectively in the altitude range between $9\,\mathrm{km}$ and $11\,\mathrm{km}$. The radiosonde data revealed an ambient-temperature of less than $-40\,^{\circ}\mathrm{C}$ at this altitude range. A comparison with calculated particle depolarization and particle lidar ratios (discussed in appendix 7.2) indicates the presence of column shaped ice particles. This assumption is supported by the Nakaya - Kobayashi diagram (Fig. 3.1) and corresponds with Nakaya (1954), Hallett and Mason (1958) and Kobayashi (1961).

5.4 Relation between particle depolarization ratios and particle lidar ratios of cirrus clouds measured between 30-07-2012 and 17-09-2012 with Polly^{XT}

The collected data from measurements of the particle depolarization ratio and particle lidar ratio of cirrus clouds over Leipzig are presented in the following. These measurements have been taken from 30-07-2012 to 17-09-2012 at the Leibniz Institute for Tropospheric Research with the portable Raman lidar system Polly^{XT}. To

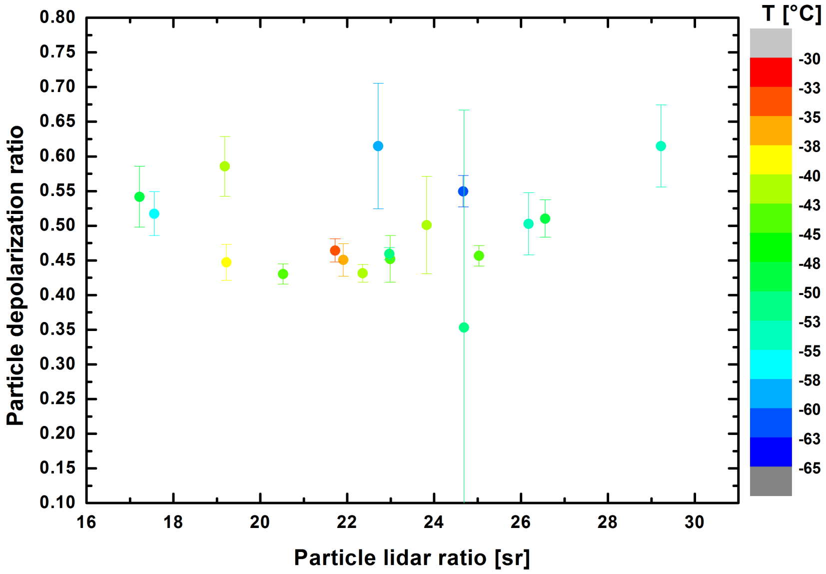

Figure 5.6: Particle depolarization ratio versus particle lidar ratio and respective ambient cloud temperature scatter-plot.

determine the air density, radiosonde data were taken from launches at Lindenberg (WMO 10393 LINDENBERG). The plot of particle depolarization ratios versus particle-lidar-ratios are shown in Fig. 5.6 with respective ambient cloud temperature. The ambient cloud temperature was less than $-40\,°\mathrm{C}$ for 15 measurements and between $-30\,°\mathrm{C}$ and $-40\,°\mathrm{C}$ for 3 measurements. All cirrus clouds were measured in an altitude range between $7\,\mathrm{km}$ and $12\,\mathrm{km}$. The retrieved data were smoothed over 13 bins, which corresponds to $390\,\mathrm{m}$. Thus, the shown particle depolarization ratios and particle lidar ratios are calculated by means of corresponding profiles starting $400\,\mathrm{m}$ above the cloud's bottom edge and ending $400\,\mathrm{m}$ under the cloud' top edge. The standard deviation from the mean particle depolarization ratio is delineated for each measurement. Based on single-scattering condition, the particle lidar ratio was derived. Due to multiple scattering, it has to be taken into account that the determined particle lidar ratios might be underestimated by up to 50%. The obtained data suggests the presence of randomly oriented column like and plate like ice crystals. This assumption corresponds with Nakaya (1954), Hallett and

Mason (1958) and Kobayashi (1961). The retrieved particle depolarization ratio implies the presence of pristine hexagonal like crystals ($\delta_{\text{par}} = 27\% - 39\%$, Guasta (2001)), hexagonal column like crystals ($\delta_{\text{par}} = 31\% - 32\%$, Hess et al. (1998); $\delta_{\text{par}} = 32\% - 33\%$, Sakai et al. (2006)), bullet rosette like crystals ($\delta_{\text{par}} \sim 33\%$, Takano and Liou (1995)), imperfect hexagonal like crystals ($\delta_{\text{par}} = 35\% - 36\%$, Hess et al. (1998)), and large column like crystals ($\delta_{\text{par}} \sim 60\%$, Cai and Liou (1982)). Due to the large influence of multiple scattering, the retrieved particle lidar ratios are not reliable to evaluate the particular crystal type. However, it must be noted that the retrieved particle lidar ratio lies in the range expected for column like crystals.

5.5 Discussion

The retrieval of the ice-crystal type out of the intensive properties particle depolarization ratio and particle lidar ratio mainly depends on a reliable multiple-scattering correction. As discussed in subchapter 3.4, cirrus clouds usually contain ice crystals with various shapes and sizes. Nevertheless, various compositions of crystal types can show similar optical properties as discussed by Macke (1993) and Yang and Liou (1998). Hence, as the distribution of column and plate shaped crystals and their size cannot be determined unequivocally, it is appropriate to designate the determined type as column like or plate like (Reichard et al., 2002). Thus, for further investigations information about the crystal size are necessary. Such information can be obtained with in-situ measurements or a multiple-FOV lidar.

A correlation of the particle depolarization ratio with the particle lidar ratio could not be determined for measured cirrus clouds over Leipzig between 30-07-2012 and 17-09-2012. Also a correlation of these optical properties with the ambient cloud temperature could not be determined. This is in contrast to Reichard et al. (2002) and Chen et al. (2002). Reichard et al. (2002) reported a separation of the particle depolarization ratio with decreasing particle lidar ratio values (Fig. 3.3). The correction of the multiple-scattering effect on the particle extinction coefficient leads to reliable particle lidar ratios. The ambient cloud temperature strengthen the assumption of a correlation for the measurements over Esrange. Although Chen et al. (2002) also reported a correlation of the particle depolarization ratio with the particle lidar ratio, an antipodal curve progression was observed (Fig. 3.4). Most of the measured cirrus clouds over Chung-Li, Taiwan are reported as subvisual thin and are not multiple-scattering corrected. As the effect of multiple scattering on the particle extinction profile is most important in the lower range of cirrus clouds and decreases with increasing depth of penetration, most of the reported particle lidar ratios might be underestimated by up to 50%. These determined optical properties in connection with the ambient cloud temperature were used to determine the crystal type as thin plate, column and thick plate. However, the particle depolarization ratio and particle lidar ratio presented in this study and the particle depolarization ratio and particle lidar ratio reported by Chen et al. (2002) and Reichard et al. (2002) correspond with Sakai et al. (2006). The comparison of measured and calculated particle depolarization ratio and particle lidar ratio over Tsukuba, Japan (Fig. 3.2) revealed that the variation of these optical properties were due to the variation of ice-crystal proportions (Sakai et al., 2006). This explains the correlation of particle depolarization ratio with particle lidar ratio as reported by Chen et al. (2002) and Reichard et al. (2002). Assuming that, the presence of only one dominant ice-crystal type is contained in the cirrus cloud, the crystal shape and size depends on supersaturation of water and the ambient cloud temperature, i.e. thin plates grow to columns with decreasing temperature and constant supersaturation. This continuous growth might lead to correlations of the particle depolarization ratio with the particle lidar ratio. The particle depolarization ratios and particle lidar ratios presented in this study are in good agreement with Sakai et al. (2006). If assuming a distribution of ice-crystal types contained in the cirrus cloud, the crystal shapes and sizes depends in different ways on supersaturation of water and ambient cloud temperature. The corresponding particle depolarization ratio and particle lidar ratio are not correlated any more, but distributed within a defined area.

6 Summary

The aim of this study was to evaluate the correlation of the particle depolarization ratio with the particle lidar ratio of cirrus clouds over Leipzig, Germany. With this correlation it would be possible to determine the types and sizes of ice crystals in cirrus clouds. The knowledge about the optical properties of ice crystals contained in cirrus clouds is the basis to estimate the radiative forcing of cirrus clouds.

At the beginning of this study, the principles and equations to retrieve the particle depolarization ratio and particle lidar ratio from measurements with an aerosol lidar have been presented. For comparison purposes, former measurement and modelling results of these optical properties of cirrus clouds depending on their micro-physical properties have been discussed in chapter 3 and data published between 1974 and 2009 have been summarized in tables in appendix 7.2. Accordingly, the ice crystal types and sizes contained in cirrus clouds are important factors to be mentioned when estimating Earth's radiation budget. Mainly depending on the optical depth of cirrus clouds and the contained ice crystal sizes, the particle extinction coefficients and thus the particle lidar ratios might be underestimated by up to 50% due to multiple-scattering effects (Wandinger, 1998; Reichard et al., 2000; Sakai et al., 2003). So, the impact of multiple scattering on lidar measurements need to be taken into consideration. A definition of cirrus clouds which is comparable to those found in literature have been used in this study and discussed in terms of altitude, optical depth and contained particles. Some of these studies revealed a correlation between the particle depolarization ratio and particle lidar ratio, but found differing interdependencies. For example, Chen et al. (2002) and Reichard et al. (2002) reported contrary relations between particle depolarization ratios and particle lidar ratios of cirrus clouds sounded in subtropical and arctic conditions, respectively whereas Sakai et al. (2006) published a broad range of these optical properties for cirrus clouds. The literature research revealed in good agreement with Sakai et al. (2006) a broad range of these optical properties for cirrus clouds.

Based on the master's thesis of Oelsner (2012), the lidar system BERTHA was equipped with a depolarization channel for the presented study to measure the particle depolarization ratios and particle lidar ratios of cirrus clouds simultaneously. This system configuration has been explained and discussed in chapter 4 and shows the capability to provide daytime and night-time measurements for retrieving particle depolarization ratios and particle lidar ratios of cirrus clouds.

A saturation effect on electronic states of iodine has been discussed for the first time in connection with its influence on measurements with the HSR channel of BERTHA and a measurement case has been used to illustrate the discrepancies at lower altitudes. This saturation effect yielded to an underestimation of the particle backscatter coefficient especially below $3\,\mathrm{km}$ altitude and a shift in the profile of the corresponding particle extinction coefficient to higher altitudes. It is caused by stray light from emitted laser light pulses. This stray light is collected by the receiver telescope and absorbed by the iodine-vapour cell. Due to the absorption a saturation of electronic states of iodine vapour is induced and thus an increase of transmittance. After that, the transmittance decreases depending on the decay time of the excited states of iodine vapour. Assuming pure iodine vapour in the cell, the decay time depends on pressure and temperature. That decay time was determined to $5\,\mu\mathrm{s}$ for the iodine-vapour cell used in the lidar system BERTHA at $35\,^{\circ}\mathrm{C}$. Therefore, the fraction of light backscattered from atmospheric particles and detected by the HSR channel has been discussed in terms of a non-negligible relaxation time of excited states of iodine vapour. A corresponding time-dependent correction function was proposed. This function concerns the described cross talk which decreases exponentially with time after a laser pulse has been emitted.

In future, further modifications of BERTHA will be carried out to reduce the measurement errors of the HSR channel and of the depolarization channel. A motorized aperture will be installed to provide multiple-FOV measurements for multiple-scattering corrections. Further channels will be installed to investigate the particle depolarization ratio at three wavelengths, the particle backscatter coefficient at three wavelengths, the particle extinction coefficient at two wavelengths, the water vapor mixing ratio, and the tropospheric temperature profile.

The particle depolarization ratio and particle lidar ratio of cirrus clouds over Leipzig, Germany were determined from measurements with the portable polarization Raman lidar system Polly^{XT} since the uncertainty in the retrieved particle depolarization ratio is smaller than this value of BERTHA. These measurements have been taken in the period between 30-07-2012 and 17-09-2012. A brief description of Polly^{XT} is given in chapter 5. The depolarization signal and the Raman signal have been measured at 532 nm wavelength and 607 nm wavelength, respectively. In contrast to Chen et al. (2002) and Reichard et al. (2002), neither a correlation of the particle depolarization ratio with the particle lidar ratio of cirrus clouds nor a correlation of these optical properties with the ambient cloud temperature could be observed. This is in good agreement with Sakai et al. (2006), who considered that these optical properties vary in a broad range assuming a distribution of ice crystals in type and size contained in the cirrus clouds. With adoption of this consideration, the correlation observed by Chen et al. (2002) and Reichard et al. (2002) can also be explained. In specific cases, where only one ice-crystal type is dominant in the cirrus cloud, its optical properties correlates with ambient cloud temperature, as for instance plates grow to columns with degreasing temperature. These cases may occur under subtropical and arctic conditions as reported by Chen et al. (2002) and Reichard et al. (2002), respectively. But in middle and northern latitudes cirrus clouds contain a distribution of ice-crystal types and sizes as reported by Sakai et al. (2006) and thus the correlation of particle depolarization ratio, particle lidar ratio and ambient cloud temperature could not be observed. However, all retrieved particle lidar ratios in this study are not corrected for multiple scattering and thus the retrieved values might be underestimated by up to 50%. Also in the literature the multiple-scattering correction is applied only partly. For example, the data retrieved by Chen et al. (2002) are published without a multiple-scattering correction and thus are comparable in their retrieval to the retrieved data in this study. However, the effect of multiple scattering has to be taken into account in further studies of the particle depolarization ratio and the particle lidar ratio of cirrus clouds. A suitable instrument for this purpose might be the redesigned lidar system BERTHA. With the proposed design the particle size can be retrieved from multiple-FOV measurements and thus an adequate multiple-scattering correction can be applied. Furthermore, the particle depolarization ratio can be determined at three wavelengths. The $45°$-calibration method is also part of the new receiver design of BERTHA. This calibration method helps minimizing the errors of the depolarization measurements.

7 Appendix

7.1 Molecular backscatter and extinction coefficient

$$\beta_{\text{mol}}(R,\lambda_i) = \sum_j n_j(R)\,\frac{d\sigma_{\text{sca},j}}{d\Omega}(\pi,\lambda_i) \tag{7.1}$$

The molecular backscatter coefficient depends on the number concentration of corresponding atoms and molecules. For an gas in hydrostatic equilibrium, the forces in vertical direction require

$$dp = -\frac{p(r)\,M\,g(r)}{R_{\text{m}}\,T_{\text{emp}}(r)}dr\ . \tag{7.2}$$

Where $M = 0.02896\,\text{kg}\,\text{mol}^{-1}$ denotes the tropospheric molar mass,
$R_{\text{m}} = 8.314\,\text{J}\,\text{K}^{-1}\text{mol}^{-1}$ is the universal gas constant, $g(r)$ is the gravitational acceleration and $T_{\text{emp}}(r)$ is the temperature. Integration from reference altitude R_0 to the altitude R_1 yields to:

$$\int\limits_{p(R_0)}^{p(R_1)} \frac{1}{p}dp = -\int\limits_{R_0}^{R_1} \frac{M\,g(r)}{R_{\text{m}}\,T_{\text{emp}}(r)}dr\ , \tag{7.3}$$

$$\frac{p(R_1)}{p(R_0)} = \exp\left\{-\int\limits_{R_0}^{R_1} \frac{M\,g(r)}{R_{\text{m}}\,T_{\text{emp}}(r)}dr\right\}\ . \tag{7.4}$$

Assuming the troposphere as an ideal gas yields to:

$$n(R_1) = n(R_0)\,\exp\left\{-\int\limits_{R_0}^{R_1} \frac{M\,g(r)}{R_{\text{m}}\,T_{\text{emp}}(r)}dr\right\} \tag{7.5}$$

and thus the molecular backscatter coefficient yields to:

$$\beta_{\text{mol}}(R,\lambda_i) = \sum_j n_j(R_0)\,\exp\left\{-\int\limits_{R_0}^{R} \frac{M\,g(r)}{R_{\text{m}}\,T_{\text{emp}}(r)}dr\right\}\frac{d\sigma_{\text{sca},j}}{d\Omega}(\pi,\lambda_i)\ . \tag{7.6}$$

According to Spuler and Mayor (2007), the differential molecular backscatter cross section can be analytically calculated to:

$$\frac{d\sigma_{\text{mol}}}{d\Omega}(\pi, \lambda_i, R) = \frac{\pi^2(\tilde{n}_{\text{air}}^2 - 1)^2}{n_{\text{air}}(R)^2 \lambda_i^4} \tag{7.7}$$

or

$$\frac{d\sigma_{\text{mol}}}{d\Omega}(\pi, \lambda_i) = 5,45 \left(\frac{550\,\text{nm}}{\lambda_i}\right)^4 10^{-32}\,\text{m}^2\text{sr}^{-1} \; . \tag{7.8}$$

Where $\tilde{n}_{\text{air}}$ denotes the tropospheric refractive index. Hence, the molecular backscatter coefficient yields to:

$$\beta_{\text{mol}}(R, \lambda_i) = n_{\text{air}}(R_0)\, \exp\left\{ - \int\limits_{R_0}^{R} \frac{M\, g(r)}{R_{\text{m}}\, T_{\text{emp}}(r)} dr \right\} \frac{\pi^2(\tilde{n}_{\text{air}}^2 - 1)^2}{n_{\text{air}}(R)^2 \lambda_i^4} \; . \tag{7.9}$$

The molecular extinction coefficient

$$\alpha_{\text{mol}}(R, \lambda_i) = \sum_j n_j(R)\, \sigma_{\text{ext},j}(\lambda_i) \tag{7.10}$$

is the product of number density and extinction cross section. In accordance to Miles et al. (2001) the extinction cross section is connected to the differential backscatter cross section by

$$\sigma_{\text{ext},j}(\lambda_i) = \frac{8\pi}{3} \frac{d\sigma_{\text{sca},j}}{d\Omega}(\pi, \lambda_i) \; . \tag{7.11}$$

Hence, the molecular extinction coefficient yields to:

$$\alpha_{\text{mol}}(R, \lambda_i) = \frac{8\pi}{3} n_i(R_0) \exp\left\{ - \int\limits_{R_0}^{R} \frac{M\, g(r)}{R_{\text{m}}\, T_{\text{emp}}(r)} dr \right\} \frac{\pi^2(\tilde{n}_{air}^2 - 1)^2}{n_i(R)^2 \lambda_i^4} \; . \tag{7.12}$$

7.2 Measured and simulated particle depolarization ratios and particle lidar ratios

Table 7.1: Comparison of observed particle depolarization ratios at 532 nm wavelength.

Value [%]	Description	Place
$0-35$	Clouds in ice-saturated air	Tsukuba, Japan (Sakai et al., 2006)
$13-18$	Cirrus at 694 nm	Middle latitudes in southern hemisphere (Platt et al., 1987)
$13-38$	Cirrus at 355 nm	Arctic (Reichard et al., 2002)
$15-55$	Cirrus at 355 nm	Esrange, Sweden (Reichard et al., 2002)
~ 18	Clouds	Antarctica (Guasta et al., 1993)
$19-27$	Cirrus	Mahé, Seychelles (Pace et al., 2003)
$20-50$	Cirrus	Chung-Li, Taiwan (Chen et al., 2002)
$21-23$	Cirrus at 694 nm	Tropics (Platt et al., 1987)
$21-62$	Optically dense midlevel Clouds, hexagonal ice	Aspendale, Australia (Young et al., 2000)
22 ± 7	Cirrus	Tsukuba, Japan (Sakai et al., 2003)
24 ± 13	Sub-visible Cirrus	Chung-Li, Taiwan (Das et al., 2009)
$\sim 25 \pm 7$	Cirrus at 694 nm	Salt Lake City, USA (Sassen and Benson, 2001)
$25-31$	Optically dense midlevel Clouds, supercooled water	Aspendale, Australia (Young et al., 2000)
27.9 ± 16	Optically thin Cirrus	Chung-Li, Taiwan (Das et al., 2009)
32 ± 19	Optically dense Cirrus	Chung-Li, Taiwan (Das et al., 2009)

Table 7.2: Comparison of calculated depolarization ratios at $532\,\mathrm{nm}$ wavelength.

Value $[\%]$	Description
0	Water droplets (Deirmendjian, 1969)
0	Horizontally orientated columns and plates (Liou and Lahore, 1974)
0	Horizontally orientated ice crystals (Sakai et al., 2006)
$<< 5$	Thin plates, aspect-ratio $\frac{L}{2a} = \frac{20}{100}$ (Guasta, 2001)
~ 10	Small crystals (in the dimension of μm) (Liou et al., 2000)
$19 - 35$	Hollow columns, aspect-ratio $\frac{L}{2a} = \frac{200}{80}$, hollow depth decreases from $100\,\mu\mathrm{m}$ to $0\,\mu\mathrm{m}$ (Takano and Liou, 1995)
$22 - 34$	Aggregates, max. dimension of $200\,\mu\mathrm{m}$ (Yang and Liou, 1998)
$22 - 36$	Plate-, bullet rosette-, dendrite-, and aggregatelike (Sakai et al., 2006)
~ 25	Small Plates, $20\,\mu\mathrm{m}$ (Cai and Liou, 1982)
$25 - 36$	Regular hexagonal plate to column, aspect-ratio $\frac{L}{2a}$ in the range of $\frac{8}{80} - \frac{400}{80}$ (Sassen and Benson, 2001)
~ 26	Dendrites, $\frac{L}{2a} = \frac{32}{80}$ (Takano and Liou, 1995)
$27 - 39$	Almost pristine hexagonal crystals (Guasta, 2001)
$31 - 32$	Hexagonal columns, max. tilt-angle $\gamma = 1^\circ$ (Hess et al., 1998)
$32 - 33$	Ice columns, tilt-angle randomly distributed between 0° and 1°, aspect-ratio $\frac{L}{2a}$ in the range of $1.25 - 5.9$ (Sakai et al., 2006)
~ 33	Bullet rosettes, $\frac{L}{2a} = \frac{120}{60}$ (Takano and Liou, 1995)
$35 - 36$	Imperfect hexagonal columns, tilt-angle $\gamma = 30^\circ$ (Hess et al., 1998)
~ 60	Large Columns, $120\,\mu\mathrm{m}$ (Cai and Liou, 1982)

Table 7.3: Comparison of observed lidar ratios at 532 nm wavelength.

Value [sr]	Description	Place
< 1	Altostratus, (horizontally oriented ice plates)	Colorado, USA (Platt, 1978)
$0.3 - 30$	Clouds in ice-saturated air	Tsukuba, Japan (Sakai et al., 2006)
$5 - 20$	Cirrus at 308 nm	Geesthacht, Germany (Ansmann et al., 1992)
$5 - 100$	Cirrus	Mahé, Seychelles (Pace et al., 2003)
$10 - 30$	Cirrus at 355 nm	Arctic (Reichard et al., 2002)
17 ± 14	Cirrus	Tsukuba, Japan (Sakai et al., 2003)
17.1 ± 15.1	Sub-visible Cirrus	Chung-Li Taiwan (Das et al., 2009)
~ 24	Cirrus at 694 nm measured with LIRAD	Salt Lake City, USA (Sassen and Comstock, 2001)
24.62 ± 11.05	Optically dense Cirrus	Chung-Li Taiwan (Das et al., 2009)
~ 25	Cirrus measured with HSRL	Wisconsin, USA (Eloranta et al., 2001)
25.94 ± 16.55	Optically thin Cirrus	Chung-Li Taiwan (Das et al., 2009)
26	Optical thin cirrus	Boulder, USA (Langford et al., 2005)
29 ± 12	Cirrus	Chung-Li, Taiwan (Chen et al., 2002)
$39 - 79$	Cirrus at 694 nm measured with LIRAD	Middle latitudes in southern hemisphere and tropics (Platt et al., 1987)
200	Subvisual cirrus at 694 nm	Salt Lake City, USA (Sassen and Cho, 1992)

Table 7.4: Comparison of calculated lidar ratios at $532\,\text{nm}$ wavelength.

Value $[sr]$	Description
< 1	Horizontally orientated ice crystals (Sakai et al., 2006)
$5 - 15$	Regular hexagonal columns and plates, aspect-ratio $\frac{L}{2a} = \frac{8}{20}, \frac{20}{20} - \frac{750}{160}, \frac{300}{120}, \frac{1000}{400}$ (Takano and Jayaweera, 1985)(Takano and Liou, 1989)(Macke, 1993)
~ 6	Aggregates, max. dimension of $200\,\mu\text{m}$ (Yang and Liou, 1998)
$6 - 19$	Plate-, bullet rosette-, dendrite-, and aggregatelike (Sakai et al., 2006)
~ 10	Bullet rosettes, aspect-ratio $\frac{L}{2a} = \frac{120}{60}$ (Takano and Liou, 1995)
~ 10	Dendrites, aspect-ratio $\frac{L}{2a} = \frac{32}{80}$ (Takano and Liou, 1995)
12	Thick-plate shaped crystals (Sassen et al., 1989)
$12 - 38$	Ice columns, tilt-angle randomly distributed between $0°$ and $1°$, aspect-ratio $\frac{L}{2a}$ in the range of $1.25 - 5.9$ (Sakai et al., 2006)
$16 - 19$	Hexagonal columns, max. tilt-angle $\gamma = 1°$ (Hess et al., 1998)
19	Water droplets (Deirmendjian, 1969)
26	Column shaped crystals (Sassen et al., 1989)
38	Thin-plate shaped crystals (Sassen et al., 1989)
$70 - 86$	Imperfect hexagonal columns, tilt-angle $\gamma = 30°$ (Hess et al., 1998)
> 120	Small crystals (a couple of micometers) (Yang and Liou, 2000)
~ 170	Hollow columns, aspect-ratio $\frac{L}{2a} = \frac{200}{100}$ with randomly depth distribution $0 - 100\,\mu\text{m}$ (Yang and Liou, 1998)

7.3 Linear-polarization dependent channel transmission

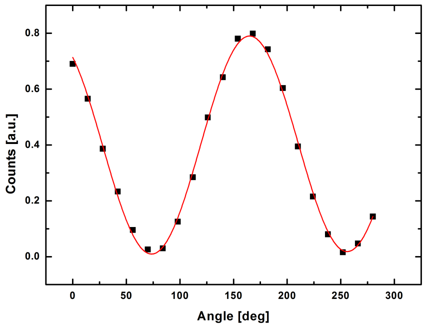

Figure 7.1: Transmission efficiency of the depolarization channel as a function of the angle of orientation of linear polarization (black squares) and the fitted Eq. 4.3 (red lined).

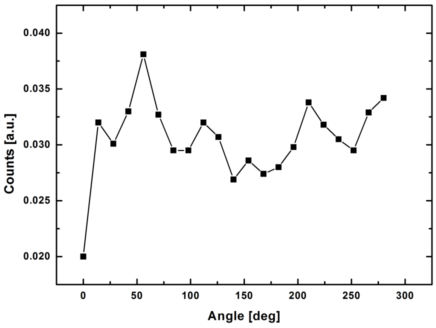

Figure 7.2: Transmission efficiency of the total channel as a function of the angle of orientation of linear polarization (black squares).

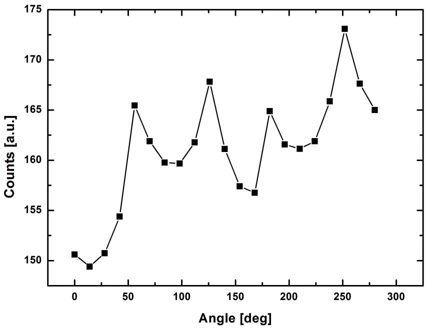

Figure 7.3: Transmission efficiency of the Raman channel as a function of the angle of orientation of linear polarization (black squares).

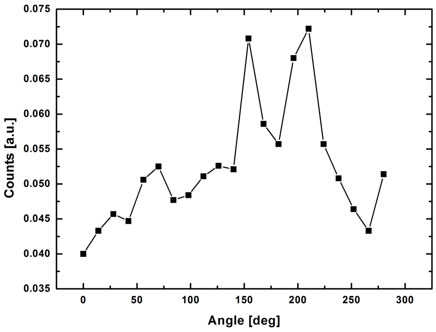

Figure 7.4: Transmission efficiency of the HSR channel as a function of the angle of orientation of linear polarization (black squares).

As discussed previously in 4.2 a combined sinusoidal linear function (red lined) is found to fit onto the transmission efficiency measurements (black squares) of the depolarization channel. The other three channels shows no sinusoidal correlation and thus Eq. 4.3 could not be applied. The observed fluctuation might be due to further effects or just statistically. An alteration of the light intensity can be neglected.

Symbol Chart

A	m^2	telescope area
a		Ångström exponent
$C^{\delta}_{\lambda_i}$		calibration constant
c	$\mathrm{m\,s}^{-1}$	speed of light in air
D_{λ_i}		transmission ratio
$D^{\perp}_{\lambda_i}$		transmission ratio of perpendicular-polarized light
G	m^{-2}	geometric factor
g	$\mathrm{m\,s}^{-2}$	gravitational acceleration
h	J s	Planck constant
I	Wm^{-2}	first Stokes parameter, light intensity
I_{sat}	$\mathrm{W\,m}^{-2}$	saturation light intensity
K	$\mathrm{J\,m^3 s}^{-1}$	system factor
$K^{\perp}$	$\mathrm{J\,m^3 s}^{-1}$	perpendicular component of system factor
k	s^{-1}	decay constant
k_{B}	$\mathrm{J\,K}^{-1}$	Boltzmann constant
M	$\mathrm{kg\,mol}^{-1}$	molar mass of the troposphere
n_i	m^{-3}	number density of scatterer
$\tilde{n}$		refractive index
O	$0 \leq O < 1$	overlap function
P	$\mathrm{J\,s}^{-1}$	lidar signal
$P_{i\,j}$	$\mathrm{J\,s}^{-1}$	Mueller matrix element
$P^{\perp}$	$\mathrm{J\,s}^{-1}$	perpendicular component of lidar signal
P_0	$\mathrm{J\,s}^{-1}$	power of emitted light
P_{HSRL}	$\mathrm{J\,s}^{-1}$	power of HSRL signal
P_{Ra}	$\mathrm{J\,s}^{-1}$	power of Raman lidar signal
p	Pa	pressure
Q	$\mathrm{W\,m}^{-2}$	second Stokes parameter

R	m	distance to scattering volume
R_0	m	reference altitude
R_{m}	$\mathrm{J\,K^{-1}mol^{-1}}$	universal gas constant
ΔR	m	spatial effective pulse length
S_{mol}	sr	molecular lidar ratio
S_{par}	sr	particle lidar ratio
T	$0 \leq T < 1$	transmission
T_{emp}	K	temperature
t	s	transit time of light
U	$\mathrm{W\,m^{-2}}$	third Stokes parameter
V	$\mathrm{W\,m^{-2}}$	fourth Stokes parameter
α	$\mathrm{m^{-1}}$	extinction coefficient
α_{abs}		absorption coefficient
α_{mol}	$\mathrm{m^{-1}}$	molecular extinction coefficient
α_{par}	$\mathrm{m^{-1}}$	particle extinction coefficient
α_{sat}		saturation broadened absorption coefficient
β	$\mathrm{m^{-1}sr^{-1}}$	backscatter coefficient
$\beta^{\parallel}$	$\mathrm{m^{-1}sr^{-1}}$	parallel component of backscatter coefficient
$\beta^{\perp}$	$\mathrm{m^{-1}sr^{-1}}$	perpendicular component of backscatter coefficient
β_{par}	$\mathrm{m^{-1}sr^{-1}}$	particle backscatter coefficient
$\beta_{\mathrm{par}}^{\parallel}$	$\mathrm{m^{-1}sr^{-1}}$	parallel component of particle backscatter coefficient
$\beta_{\mathrm{par}}^{\perp}$	$\mathrm{m^{-1}sr^{-1}}$	perpendicular component of particle backscatter coefficient
β_{mol}	$\mathrm{m^{-1}sr^{-1}}$	molecular backscatter coefficient
$\beta_{\mathrm{mol}}^{\parallel}$	$\mathrm{m^{-1}sr^{-1}}$	parallel component of molecular backscatter coefficient
$\beta_{\mathrm{mol}}^{\perp}$	$\mathrm{m^{-1}sr^{-1}}$	perpendicular component of molecular backscatter coefficient
γ	$\mathrm{rad\,s^{-1}}$	angular frequency FWHM
γ_{sat}	$\mathrm{rad\,s^{-1}}$	saturation broadened angular frequency FWHM
δ_{mol}		molecular depolarization ratio
δ_{par}		particle depolarization ratio

δ_{vol}		volume depolarization ratio
η	$0 \leq \eta < 1$	system efficiency
$\eta^{\perp}$	$0 \leq \eta < 1$	system efficiency for perpendicular-polarized light
κ_{m}		cross talk parameter for molecular HSR signal
κ_{p}		cross talk parameter for particle HSR signal
λ_0	nm	wavelength of emitted light
λ_i	nm	wavelength of received light
ν	Hz	frequency
σ_{abs}	m^2	absorption cross section
σ_{ext}	m^2	extinction cross section
σ_{sca}	m^2	scattering cross section
$\frac{d\sigma_{\text{sca}}}{d\Omega}$	m^2sr^{-1}	differential scattering cross section
τ	s	temporal pulse length
τ_{dec}	s	mean decay time
ω	$\text{rad}\,\text{s}^{-1}$	angular frequency
ω_0	$\text{rad}\,\text{s}^{-1}$	central angular frequency

List of abbreviations

BERTHA	Backscatter, Extinction, lidar Ratio, Temperature, Humidity profiling Apparatus
FOV	Field Of View
FWHM	Full Width at Half Maximum
HSR	High Spectral Resolution
HSRL	High Spectral Resolution LIDAR
LIDAR	Light Detection And Ranging
PMT	Photo Multiplier Tube
Polly^{XT}	POrtable Lidar sYstem eXTended
RADAR	Radio Detection And Ranging
UPS	Uninterruptible Power Supply

Bibliography

Ångstöm, A. (1964). The parameters of atmospheric turbidity. *Tellus Series*, 16:64 – 75.

Althausen, D., Engelmann, R., Baars, H., Heese, B., Ansmann, A., Müller, D., and Komppula, M. (2009). Portable Raman lidar PollyXT for automated profiling of aerosol backscatter, extinction, and depolarization. *Journal of Atmospheric and Oceanic Technology*, 26:2366 – 2378.

Althausen, D., Müller, D., Ansmann, A., Wandinger, U., Hube, H., Clauder, E., and Zörner, S. (2000). Scanning 6-Wavelength 11-Channel Aerosol Lidar. *American Meteorological Society*, 17:1469 – 1482.

Ansmann, A. and Müller, D. (2005). *Lidar Range-Resolved Optical Remote Sensing of the Atmosphere*, chapter Lidar and Atmospheric Aerosol Particles, pages 105 – 141. Springer Science + Business Media Inc.

Ansmann, A., Riebesell, M., and Weitkamp, C. (1990). Measurement of atmospheric aerosol extinction profiles with a Raman lidar. *Optics Letters*, 15:746 – 748.

Ansmann, A., Wandinger, U., Riebesell, M., Weitkamp, C., and Michaelis, W. (1992). Independent measurement of extinction and backscatter profiles in cirrus clouds by using a combined Raman elastic-backscatter lidar. *Applied Optics*, 31:7113 – 7131.

Asano, S. (1983). Transfer of Solar Radiation in Optically Anisotropic Ice Clouds. *Journal of the Meteorological Society of Japan*, 61:402 – 413.

Autodesk Inc. (2012). Autodesk Inventor 2013.

Baars, H. (2012). *Aerosol profiling with lidar in the Amazon Basin during the wet and dry season 2008*. PhD thesis, Leibniz Institute for Tropospheric Research, Leipzig.

Cai, Q. and Liou, K.-N. (1982). Polarized light scattering by hexagonal ice crystals: theory. *Applied Optics*, 21:3569 – 3580.

Cairo, F., di Donfrancesco, G., Adriani, A., Pulvirenti, L., and Fierli, F. (1999). Comparison of various linear depolarization parameters measured by lidar. *Applied Optics*, 38:4425 – 4432.

Chen, W.-N., Chiang, C.-W., and Nee, J.-B. (2002). Lidar ratio and depolarization ratio for cirrus clouds. *Applied Optics*, 41:6470 – 6476.

Das, S. K., Chiang, C.-W., and Nee, J.-B. (2009). Characteristics of cirrus clouds and its radiative properties based on lidar observation over Chung-Li, Taiwan. *Atmospheric Research*, 93:723 – 735.

Deirmendjian, D. (1969). *Electomagnetic Scattering on Spherical Polydispersions*, page 78. Elsevier.

Demtröder, W. (2000). *Laserspektroskopie: Grundlagen und Techniken*. Springer-Verlag.

Eloranta, E., Kuehn, R., and Holz, R. (2001). Measurements of Backscatter Phase Function and Depolarization in Cirrus Clouds made with the University of Wisconsin High Spectral Resolution Lidar. In *Advances in Laser Remote Sensing*, pages 255 – 257.

Eloranta, E. W. and Kuehn, R. E. (2002). Multiple Scattering Determinations of Particle Size in Cirrus Clouds.

Engelmann, R., Althausen, D., Heese, B., Baars, H., and Komppula, M. (2012). Recent Upgrades of the Multiwavelength Polarization Raman Lidar Polly^{XT}. In *Reviewed and Revised Papers of the 26th International Laser Radar Conference*.

Fernald, F. G. (1984). Analysis of atmospheric lidar observations: some comments. *Applied Optics*, 23:652 – 653.

Fiocco, G. and Smullin, L. (1963). Detection of scattering layers in the upper atmosphere (60-140 km) by optical radar. *Nature*, 199:1275 – 1276.

Freudenthaler, V., Esselborn, M., Wiegner, M., Heese, B., Tesche, M., Ansmann, A., Müller, D., Althausen, D., Wirth, M., Fix, A., Ehret, G., Knippertz, P., Toledano, C., Gasteiger, J., Garhammer, M., and Seefelder, M. (2009). Depolarization ratio profiling at several wavelengths in pure Saharan dust during SAMUM 2006. *Tellus Series*, B, 61:165 – 179.

Grein, M. (2006). Charakterisierung und Erweiterung der Empfängeroptik des IfT-Ramanlidars MARTHA für kombinierte Aerosol- und Wolkenmessungen. Master's thesis, Leibniz-Institute for Tropospheric Research, Leipzig.

Guasta, M. D. (2001). Simulation of LIDAR returns from pristine and deformed hexagonal ice prisms in cold cirrus by means of "face tracing". *Journal of Geophysical Research*, 106:12,589 – 12,602.

Guasta, M. D., Morandi, M., and Stefanutti, L. (1993). One Year of Cloud Lidar Data From Dumont d'Urville (Antarctica) 1. General Overview of Geometrical and Optical Properties. *Journal of Geophysical Research*, 98:18575 – 18587.

Hallett, J. and Mason, B. (1958). The Influence of Temperature and Supersaturation on the Habit of Ice Crystals Grown from the Vapour. *Proceedings of the Royal Society of London*, 247:440 – 453.

Harms, J. and Weitkamp, C. (1978). Geometrical compression of lidar return signals. *Applied Optics*, 17:1131 – 1135.

Hess, M., Koelemeijer, R. B., and Stammes, P. (1998). Scattering matrices of imperfect hexagonal ice crystals. *Journal of Quantitative Spectroscopy and Radiative Transfer*, 60:301 – 308.

Klett, J. (1981). Stable analytical inversion solution for processing lidar returns. *Applied Optics*, 20:211 – 220.

Kobayashi, T. (1961). The growth of snow crystals at low supersaturations. *Philosophical Magazine*, 6:1363 – 1370.

Langford, A., Portmann, R., Daniel, J., Miller, H., Eubank, C., Solomon, S., and Dutton, E. (2005). Retrieval of ice crystal effective diameters from ground-based near-infrored spectra of optically thin cirrus. *Journal of Geophysical Research*, 110:D22201 1 – 11.

Libbrecht, K. G. (2001). *Engineering and Science*, chapter Morphogenesis on Ice: The Physics of Snow Crystals, pages 10 – 19. California Institute of Technology.

Ligda, M. (1963). Proceedings of the First Conference on Laser Technology. San Diego CA. U.S. Navy Office of Naval Research.

Liou, K. and Lahore, H. (1974). Laser Sensing of Cloud Composition: A Backscattered Depolarization Technique. *Journal of Applied Meteorology*, 13:257 – 263.

Liou, K., Takano, Y., and Yang, P. (2000). *Light Scattering and Radiative Transfer in Ice Crystal Clouds*, chapter Applications to Climate Research, pages 417 – 449. Academic, San Diego, California.

Liou, K.-N. (1986). Influence of cirrus clouds on weather and climate processes: A global perspective. *Monthly Weather Review*, 114:1167 – 1198.

Macke, A. (1993). Scattering of light by polyhedral ice crystals. *Applied Optics*, 32:2780 – 2788.

Masiello, T., Vulpanovici, N., and Nibler, J. W. (2003). Fluorescence Lifetime and Quenching of Iodine Vapor. *Journal of Chemical Education*, 80:914 – 917.

Mattis, I. (2002). *Aufbau eines Feuchte-Temperatur-Aerosol-Ramanlidars und Methodenentwicklung zur kombinierten Analyse von Trajektorien und Aerosolprofilen*. PhD thesis, University of Leipzig.

Mattis, I., Tesche, M., Grein, M., Freudenthaler, V., and Müller, D. (2009). Systematic error of lidar profiles caused by a polarization-dependent receiver transmission: Quantification and error correction scheme. *Applied Optics*, 48:2742 – 2751.

Middleton, W. and Spilhaus, A. (1953). *Meteorological Instruments*. University of Toronto Press.

Miles, R. B., Lempert, W. R., and Forkey, J. N. (2001). Laser Rayleigh scattering. *Institute of Physics Publishing*, 12:33 – 51.

Murayama, T., Okamoto, H., Kaneyasu, N., Kamataki, H., and Miura, K. (1999). Application of lidar depolarization measurement in the atmospheric boundary layer: Effects of dust and sea-salt particles. *Journal of Geophysical Research*, 104:31781 – 31792.

Nakaya, U. (1954). *Snow Crystals: Natural and Artificial*. Harvard University Press.

Oelsner, P. (2012). Aufbau eines High-Spectral-Resolution-Kanals und Vergleich mit dem Raman-Kanal eines Aerosol-Lidars. Master's thesis, Universität Leipzig.

Pace, G., Cacciani, M., di Sarra, A., Fiocco, G., and Fuà, D. (2003). Lidar observations of equatorial cirrus clouds at Mahè, Seychelles. *Journal of Geophysical Research*, 108:AAC 2–1 – AAC 2–11 and AAC 4–4 – AAC 4–6.

Platt, C. (1978). Lidar backscatter from horizontal ice crystal plates. *Journal of Applied Meteorology*, 17:482 – 488.

Platt, C., Scott, J., and Dilley, A. (1987). Remote Sounding of High Clouds. Part VI: Optical Properties of Midlatitude and Tropical Cirrus. *American Meteorological Society*, 44:729 – 747.

Reichard, J., Hess, M., and Macke, A. (2000). Lidar inelastic multiple-scattering parameters of cirrus particle ensembles determined with geometrical-optics crystal phase functions. *Applied Optics*, 39:1895 – 1910.

Reichard, J., Reichardt, S., Hess, M., and McGee, T. (2002). Correlations among the optical properties of cirrus-cloud particles: Microphysical interpretation. *Journal of Geophysical Research*, 107:AAC 8–1 – AAC 8–12.

Sakai, T., Nagai, T., Nakazato, M., Mano, Y., and Matsumura, T. (2003). Ice clouds and Asian dust studied with lidar measurements of particle extinction-to-backscatter ratio, particle depolarization, and water-vapor mixing ratio over Tsukuba. *Applied Optics*, 42:7103 – 7116.

Sakai, T., Orikasa, N., Nagai, T., Murakami, M., Kusunoki, K., Mori, K., Hashimoto, A., Matsumura, T., and Shibata, T. (2006). Optical and Microphysical Properties of Upper Clouds Measured with the Raman Lidar and Hydrometeor Videosonde: A Case Study on 29 March 2004 over Tsukuba, Japan. *Journal of the Atmospheric Sciences*, 63:2156 – 2166.

Sassen, K., Arnott, W. P., Barnett, J. M., and Aulenbach, S. (1998). Can cirrus clouds produce glories? *Applied Optics*, 37:1427 – 1433.

Sassen, K. and Benson, S. (2001). A Midlatitude Cirrus Cloud Climatology from the Facility for Atmospheric Remote Sensing. Part II: Microphysical Properties Derived from Lidar Depolarization. *Journal of the Atmospheric Sciences*, 58:2103 – 2112.

Sassen, K. and Cho, B. S. (1992). Subvisual-Thin Cirrus Lidar Dataset for Satellite Verification and Climatological Research. *Journal of Applied Meteorology*, 31:1275 – 1285.

Sassen, K. and Comstock, J. (2001). A midlatitude cirrus cloud climatology from the Facility for Atmospheric Remote Sensing: III: Radiative properties. *Journal of the Atmospheric Sciences*, 58:2113 – 2127.

Sassen, K., Griffin, M. K., and Dodd, G. C. (1989). Optical Scattering and Microphysical Properties of Subvisual Cirrus Clouds, and Climatic Implications. *Journal of Applied Meteorology*, 28:91 – 98.

Schuldt, T. (2003). Frequenzstabilisierter Nd:YAG-Laser für Weltraumanwendungen. Master's thesis, Universität Hamburg.

Spuler, S. M. and Mayor, S. D. (2007). Eye-safe aerosol lidar at 1.5 microns: progress towards a scanning lidar network. *Proceedings of SPIE*, 6681.

Stephens, G. L., Tsay, S.-C., Jr., P. W. S., and Flatau, P. J. (1990). The Relevance of the Microphysical and Radiative Properties of Cirrus Clouds to Climate and Climatic Feedback. *Journal of the Atmospheric Sciences*, 47:1742 – 1753.

Takano, Y. and Jayaweera, K. (1985). Scattering phase matrix for hexagonal ice crystals computed from ray optics. *Applied Optics*, 24:3254 – 3263.

Takano, Y. and Liou, K. (1995). Radiative Transfer in Cirrus Clouds. Part III: Light Scattering by Irregular Ice Crystals. *Journal of the Atmospheric Sciences*, 52:818 – 837.

Takano, Y. and Liou, K.-N. (1989). Solar Radiative Transfer in Cirrus Clouds. Part I: Single-Scattering and Optical Properties of Hexagonal Ice Crystals. *Journal of the Atmospheric Sciences*, 46:3 – 19.

Tesche, M. (2011). *Vertical profiling of aerosol optical properties with multiwavelength aerosol lidar during the Saharan Mineral Dust Experiments*. PhD thesis, Universität Leipzig.

van de Hulst, H. (1981). *Light Scattering by Small Particles*, page 407. Dover Publications, Inc.

Wandinger, U. (1994). *Theoretische und experimentelle Studien zur Messung stratosphärischen Aerosols sowie zum Einfluß der Mehrfachstreuung auf Wolkenmessungen mit einem Polarisations-Raman-Lidar*. PhD thesis, Universität Hamburg.

Wandinger, U. (1998). Multiple-scattering influence on extinction and backscatter-coefficient measurements with Raman and High-Spectral-Resolution Lidars. *Applied Optics*, 37:417 – 427.

Wandinger, U. (2005a). *Lidar Range-Resolved Optical Remote Sensing of the Atmosphere*, chapter 1.4 Lidar Equation, page 7. Springer Science + Business Media Inc.

Wandinger, U. (2005b). *Lidar Range-Resolved Optical Remote Sensing of the Atmosphere*, chapter Raman Lidar, pages 241 – 267. Springer Science + Business Media Inc.

Wylie, D. P., Menzel, W. P., Woolf, H. M., and Strabala, K. I. (1994). Four Years of Global Cirrus Cloud Statistics Using HIRS. *American Meteorological Society*, 7:1972 – 1986.

Yang, P. and Liou, K. (1998). Single-Scattering Properties of Complexe Ice Crystals in Terrestrial Atmosphere. *Contributions to Atmospheric Physics*, 71:223 – 248.

Yang, P. and Liou, K.-N. (2000). *Light Scattering by Nonspherical Particles: Theory, Measurements and Applications*, chapter Finite Difference Time Domain Mehod for Light Scattering by Nonspherical and Inhomogeneous Particles, pages 173 – 221. Academic, San Diego, California.

Young, S., Platt, C., Austin, R., and Patterson, G. (2000). Optical Properties and Phase of Some Midlatitude, Midlevel Clouds in ECLIPS. *Journal of Applied Meteorology*, 39:135 – 153.

Zemax Development Corporation (2010). Zemax. Radiant Zemax LLC.

Danksagung

An dieser Stelle möchte ich mich bei all jenen bedanken, die mir diese Arbeit ermöglicht haben.

Ohne sein großes Vertrauen und seine intensive Betreuung hätte ich nicht einmal mit dieser Arbeit beginnen können. Mein Betreuer am Leibniz-Institut für Troposphärenforschung in Leipzig, Dr. Dietrich Althausen, gab mir die Möglichkeit meine Ideen verwirklichen zu können und nahm sich die Zeit mir eine intensive Betreuung zukommen zu lassen. Ihm und Frau Dr. Birgit Heese danke ich für die große Mühe meine Arbeit Korrektur zu lesen. Prof. Dr. Friedrich Kremer möchte ich für seine angenehme Betreuung an der Universität Leipzig danken. Allen Mitarbeitern der Lidargruppe möchte ich danken für die offene und familiäre Atmosphäre. Ich hatte immer das Gefühl, dass ich mit Hilfestellungen und Erklärungen bei auftretenden Problemen rechnen konnte. Für sein Programm zur Datenauswertung möchte ich mich bei Dr. Holger Baars bedanken. Er und Jörg Schmidt haben mir oft mit aufmunternden Worten zur Seite gestanden. Mit viel Geduld hat Dr. Ronny Engelmann mir versucht sein Wissen zu vermitteln auch wenn ich oft wegen ähnlicher Probleme zu ihm kommen musste. Für ihre große Unterstützung bei der Auswertung der PollyXT-Daten möchte ich Maren Haid danken.

Ich hätte diese Arbeit nicht schreiben können ohne die liebevolle Fürsorge meiner Freundin Lisa de Meer. Auch meinen Eltern und meiner Familie bin ich dankbar, dass sie mir dieses Studium ermöglicht haben und mir immer den notwendigen Rückhalt gaben den ich oft auch brauchte.

Erklärung

Hiermit erkläre ich, dass ich die Diplomarbeit selbständig verfasst habe und keine anderen als die angegebenen Quellen und Hilfsmittel benutzt habe. Alle Stellen der Arbeit, die wörtlich oder sinngemäß aus Veröffentlichungen oder aus anderweitigen fremden Äußerungen entnommen wurden, sind als solche kenntlich gemacht. Ferner erkläre ich, dass die Arbeit noch nicht in einem anderen Studiengang als Prüfungsleistung verwendet wurde.

....
Unterschrift des Verfassers

Ich bin einverstanden, dass die Arbeit nach positiver Begutachtung in der Universitätsbibliothek zur Verfügung steht.

....
Unterschrift des Verfassers